

Probing radio source environments via H_I and OH absorption

Neeraj Gupta¹*, C.J. Salter², D.J. Saikia^{1,3}, T. Ghosh² and S. Jeyakumar⁴

¹ NCRA, TIFR, Post Bag 3, Ganeshkhind, Pune 411 007, India

² Arecibo Observatory, NAIC, HC3 Box 53995, Arecibo, Puerto Rico PR 00612, USA

³ Jodrell Bank Observatory, University of Manchester, Macclesfield, Cheshire SK11 9DL

⁴ Instituto de Geofisica, UNAM, Mexico

Accepted. Received; in original form

ABSTRACT

We present the results of H_I and OH absorption measurements towards a sample of radio sources using the Arecibo 305-m telescope and the Giant Metrewave Radio Telescope (GMRT). In total, 27 radio sources were searched for associated 21-cm H_I absorption. One totally new H_I absorption system was detected against the radio galaxy 3C258, while five previously known H_I absorption systems, and one galaxy detected in emission, were studied with improved frequency resolution and/or sensitivity. Our sample included 17 gigahertz peaked spectrum (GPS) and compact steep spectrum (CSS) objects, 4 of which exhibit H_I absorption. This detection rate of $\sim 25\%$ compares with a value of $\sim 40\%$ by Vermeulen et al. for similar sources. We detected neither OH emission nor absorption towards any of the sources that were observed at Arecibo. We are, however, able to estimate a limit on the abundance ratio of $N(\text{H}_\text{I})/N(\text{OH}) \gtrsim 4 \times 10^6$ for 3C258.

We have combined our results with those from other available H_I searches to compile a heterogeneous sample of 96 radio sources consisting of 27 GPS, 35 CSS, 13 compact flat spectrum (CFS) and 21 large (LRG) sources. The H_I absorption detection rate is highest ($\sim 45\%$) for the compact GPS sources and least for the LRG sources. We find H_I column density to be anticorrelated with source size, as reported earlier by Pihlström et al., a trend which is consistent with the results of optical spectroscopy. The H_I column density shows no significant dependence on either redshift or luminosity, which are themselves strongly correlated. These results suggest that the environments of radio sources on GPS/CSS scales are similar at different redshifts. Further, in accordance with the unification scheme, the GPS/CSS galaxies have an H_I detection rate of $\sim 40\%$ which is higher than the detection rate ($\sim 20\%$) towards the GPS/CSS quasars. Also, the principal (strongest) absorption component detected towards GPS sources appears blue-shifted in $\sim 65\%$ of the cases. This is in agreement with the growing evidence for jet-cloud interactions playing an important role in determining the ionization and kinematical properties of the ambient gas.

Key words: galaxies: active – galaxies: evolution – galaxies: nuclei – galaxies: absorption lines – radio lines: galaxies – galaxies: individual: 3C258

1 INTRODUCTION

There is general agreement that the energy output from an active galactic nucleus (AGN) is fuelled by the supply of gas to the central engine, which is presumably a supermassive black hole (e.g. Rees 1984). This infall could be triggered by

interactions or mergers with companion galaxies, leading to the formation of circumnuclear starbursts and the fuelling of nuclear black holes (e.g. Sanders et al. 1988). Although there have been a number of studies of the gas kinematics of nearby AGN in an effort to understand both the fuelling of this activity and the relationship between the starburst and the AGN, relatively little is known regarding the situation in powerful radio galaxies. Observationally, there is evidence that the central regions of such galaxies contain dust plus ionised, atomic and molecular gas which could be reser-

* E-mail: neeraj@ncra.tifr.res.in (NG); csalter@naic.edu (CJS); djs@ncra.tifr.res.in (DJS); tghosh@naic.edu (TG); sjk@geofisica.unam.mx (SJ)

Table 1. Radio sources observed with the Arecibo telescope and GMRT.

Source name	Alt. name	Opt. id.	Redshift	$S_{5\text{GHz}}$	$\alpha_{1.4}^5$	Spect. class	$P_{5\text{GHz}} 10^{25}$ W/Hz	Str. class	LAS	LLS	Ref.	Radio class
(1)	(2)	(3)	(4)	Jy (5)	(6)	(7)	(8)	(9)	" (10)	kpc (11)	(12)	(13)
J0031-2652	MRC	Q	0.333	0.12	1.03	STP	4.4	U	<1	<4.8	1	CSS
J0034+3025	B2	G	0.1744	0.07	1.06	STP	0.7	SR	~1.3	2.9	2	CSS
J0040-2043	MRC	G	0.091	0.34	0.51	STP	0.7	CE	<2.4(15)	<4.0(25.5)	0	CSS
J0119+3210	4C+31.04	G	0.060	1.58	0.47	LFT	1.3	T	0.08	0.1	4	CSS
J0137+3309	3C48	Q	0.3700	5.73	0.82	LFT	245	T	1.2	6.12	5	CSS
J0251+4315	S4	Q	1.311	1.43	-0.45	GPS	449	T?	0.0124	0.11	6	GPS
J0255-2153	MRC	G	0.1128	0.17	0.97	STP	0.58	U	<2	<4.0	3	CSS
J0301+3512	NGC1167	G	0.0165	0.86	0.58	STP	0.1	T?	1.13	0.3	7	CSS
J0347-2900	MRC	G	0.1423	0.30	0.90	STP	1.54	U	<5	<12.5	3	CSS
J0513+0157	4C+01.13	BL/G	0.0881 [†]	0.14	0.40	FLT*	0.2	SR	61.2	97.9	8	LRG
J0645+2121	3C166	G	0.2449	1.24	0.58	STP	19.9	T	45.0	171	9	LRG
J0725-0054	PKS	G	0.1273	1.38	0.01	FLT	4.9	CJ	0.03	0.07	10	CFS
J0805+2409	3C192	G	0.0598	1.86	0.88	STP	1.5	T	200	220	11	LRG
J0822+0557	3C198	G	0.08156	0.44	1.13	STP	0.7	D	198	297	12	LRG
J0901+2901	3C213.1	G	0.194	0.78	0.53	STP	7.4	T	5.7(40)	18.2(128)	13	LRG
J1124+1919	3C258	G	0.165	0.45	0.60	STP	3.0	D	0.10(60)	0.28(168)	7,14	CSS
J1148+5924	NGC3894	G	0.01075	0.62	-0.31	FLT	0.02	T	0.04	0.008	15	CFS
J1347+1217	4C+12.50	Sy/Q	0.12174	3.10	0.45	LFT	10.8	T	0.09	0.20	16	CSS
J1407+2827	Mrk668	Sy	0.0766	2.41	0.87	GPS	3.1	D?	0.008	0.01	17	GPS
J1516+0015	MRC	G	0.052	1.64	0.40	FLT*	0.98	CJ	0.009	0.01	18	CFS
J1521+0430	4C+04.51	Q	1.296	1.19	1.05	GPS	1208	D	0.137	1.15	19	GPS
J1604-2223	MRC	G	0.141	0.39	0.67	GPS	1.9	D	0.013	0.03	18	GPS
J1643+1715	3C346	G	0.162	1.39	0.78	STP	9.3	T	13.3	37.2	4,13	LRG
J2058+0542	4C+05.78	G	1.381	0.36	0.98	LFT	402	U	<0.4	<3.4	20	CSS
J2250+1419	4C+14.82	Q	0.23478	1.18	0.47	STP	16.8	D	0.2	0.74	21	CSS
J2316+0405	3C459	G	0.2199	1.43	0.95	LFT	19.2	D	8.0	28.0	22	LRG
J2325+4346	OZ438	G	0.145	0.92	0.63	STP	4.7	D	1.6	4.0	7	CSS

Col. 1: source name; col. 2: alternative name; col. 3: optical identification, where BL = BL Lac object, G = galaxy, Q = quasar and Sy = Seyfert galaxy; col. 4: redshift; col. 5: total 5-GHz flux density; col. 6: spectral index between 1.4 and 5 GHz; col. 7: integrated radio spectral class, where STP = steep, i.e. $\alpha \geq 0.5$, LFT = low-frequency turnover, GPS = gigahertz peaked and FLT = flat spectrum; col. 8: 5-GHz luminosity in the rest frame of the source; col. 9: radio structure classification, where CE = unresolved component with extended emission, CJ = core-jet source, D = double-lobed, SR = slightly resolved, T = triple and U = unresolved (deconvolved size \lesssim a fifth of the resolution element); cols. 10 & 11: largest projected angular (LAS) and linear (LLS) size in arcsec and kpc respectively, as measured from the outermost radio peaks, or from Gaussian fits to slightly resolved sources; col. 12: references for the radio structure and col. 13: radio class, where CSS = compact steep-spectrum, GPS = gigahertz peaked-spectrum, CFS = compact flat-spectrum, and LRG = large radio source; see text (Section 2.1) for further details.

References for the largest angular sizes – 0: This paper; 1: Kapahi et al. (1998b); 2: Saikia et al. (2002); 3: Kapahi et al. (1998a); 4: Cotton et al. (1995); 5: Feng et al. (2005); 6: Fey & Charlton (2000); 7: Sanghera et al. (1995); 8: NRAO VLA Sky Survey (NVSS) at 1.4 GHz; 9: Neff, Roberts & Hutchings (1995); 10: Bondi et al. (1996); 11: Baum et al. (1988); 12: Fomalont & Bridle (1978); 13: Akujor & Garrington (1995); 14: Strom et al. (1990); 15: Peck & Taylor (1998); 16: Lister et al. (2003); 17: Stanghellini et al. (2001); 18: Beasley et al. (2002); VCS observations; 19: Xiang et al. (2002); 20: de Breuck et al. (2000); 21: Spencer et al. (1989); 22: Thomasson, Saikia & Muxlow (2003)

[†] The source was observed at $z = 0.084$, the best available redshift at that time.

* The intergrated spectrum exhibits low-frequency steepening.

voirs of fuel for the central engine. For example, Walsh et al. (1989) have shown that long-wavelength infrared emission, indicative of dust, is correlated with nuclear radio emission. Further, Verdoes Kleijn et al. (1999), from an HST study of 19 Fanaroff-Riley class I (FRI) galaxies, have demonstrated the presence of dust structures in 17 of these. Besides such structures, atomic and molecular gas within $\sim 5\text{--}10$ kpc of the nuclear region has been seen in many nearby active galaxies, including several well-known radio galaxies (e.g. Rupen 1997; Lim et al. 2000; Leon et al. 2003).

In the canonical model of an AGN, the nuclear region

contains a torus around a supermassive black hole. The torus can consist of ionised, atomic and molecular gas components. An understanding of the distribution and kinematics of the different components of the circumnuclear gas is important both for studying the anisotropy in the radiation field and thereby testing the unified scheme, and for understanding the fuelling of the radio activity. In addition, detection of this gas over a large range of redshifts and source sizes can provide valuable information on the evolution of its properties with redshift and source size (age). At radio wavelengths, the ionized component of this gas may

Table 2. Observational details and results of the Arecibo search for associated HI absorption.

Source name (1)	S _{1.4GHz} Jy (2)	Date (3)	Δv ^{HI} km s ⁻¹ (4)	σ _{FA} ^{HI} 10 ⁻³ (5)	FA _{max} (6)	W _{50%} km s ⁻¹ (7)	N(HI) 10 ²⁰ cm ⁻² (8)
J0034+3025	0.26	2002 Dec	16.0	2.0	—	—	<1.16
J0119+3210	2.64	2002 Dec	0.72 ^a	1.5 ^a 0.030 ^d	0.038 ^b 7.6 ^d	153 ^b —	12.2±0.14 ^c
J0301+3512	1.84	2002 Dec	24.0	1.3	—	—	<0.75
J0513+0157	0.35	2004 Mar	13.6	2.7	—	—	<1.56
J0645+2121	2.59	2002 Dec	18.0	0.85	—	—	<0.49
		2004 Sep					
J0725-0054	1.40	2002 Dec	14.8	3.6	—	—	<2.08
J0805+2409	5.33	2002 Dec	13.0	0.62	—	—	<0.36
J0822+0557	1.98	2002 Dec	13.6	1.4	—	—	<0.81
J0901+2901	2.00	2002 Nov	16.5	0.46	—	—	<0.27
		2002 Dec					
J1124+1919	0.88	2002 Nov	3.5	1.3	0.095	31.5	5.05±0.13
		2003 Jan					
J1347+1217	5.40	2002 Nov	3.2	0.87	0.012	135	3.03±0.16
		2003 Jan					
J1407+2827	0.82	2002 Nov	13.4	0.66	0.003	326	1.53±0.29
		2003 Jan					
J2250+1419	1.97	2002 Dec	17.7	0.40	—	—	<0.23
J2316+0405	4.68	2002 Dec	17.2	0.49	0.0034	166	1.33±0.27
		2005 Aug					

Col. 1: source name; col. 2: 1.4-GHz flux density from NASA/IPAC Extragalactic Database (NED); col. 3: dates of observation; col. 4 & 5: the smoothed velocity resolution and the corresponding 1- σ noise for the HI fractional absorption; cols. 6 & 7: peak optical depth and full width at half maximum (FWHM) for the absorption components derived directly from spectra with the velocity resolution given in col. 5, and col. 8: HI column density assuming T_s=100 K. Upper limits and quoted errors are both 3 σ . The upper limits assume Δv=100 km s⁻¹ and f_c=1.0.

^a These values are for a spectrum with a total bandwidth of 3.125 MHz. The values for a total bandwidth of 25 MHz were σ_{FA}^{HI}=0.00051 and Δv^{HI}=5.8 km s⁻¹.

^b The maximum optical depth and velocity half width given represent just the main absorption component.

^c The integrated column density is for the total absorption spectrum.

^d The maximum optical depth and velocity half width given represent just the secondary absorption component.

be probed via radio polarization measurements of compact source components residing within the dense interstellar environments of their parent galaxies. Radio cores, and compact steep-spectrum (CSS) and gigahertz peaked-spectrum (GPS) sources constitute such objects. CSS sources are defined as those with a projected linear size \lesssim 15 kpc (H_o=71 km s⁻¹ Mpc⁻¹, Ω_m=0.27, Ω_Λ=0.73, Spergel et al. 2003) and having a steep high-frequency radio spectrum ($\alpha \gtrsim 0.5$, where S(ν) $\propto \nu^{-\alpha}$). The structural and polarization asymmetries observed in these sources require an asymmetric distribution of gas in the central regions of the galaxy, which may be related to the infall of gas that fuels the radio source (Saikia et al. 1995; Saikia & Gupta 2003, and references therein).

An important way of probing atomic gas on sub-galactic scales is via HI absorption towards the compact components of CSS and GPS sources or the radio nuclei of larger objects (e.g. van Gorkom et al. 1989; Conway & Blanco 1995; Peck et al. 2000; Pihlström 2001; Vermeulen et al. 2003; Pihlström, Conway & Vermeulen 2003). A pioneering study of HI absorption for a well-defined sample of radio galaxies was made by van Gorkom et al. (1989). This detected HI in 4 out of 29 galaxies, all 4 being dominated by a compact nuclear radio source. More recently, a large survey of CSS and GPS sources detected HI absorption in 33%, with the HI column density being anti-correlated with source size

(Vermeulen et al. 2003; Pihlström et al. 2003). The HI spectra exhibit a variety of line profiles, implying significant, sometimes complex, gas motions. van Gorkom et al. (1989) had reported that the HI-absorption features tend to be redshifted from the systemic velocity, suggesting infall of gas. However, recent observations show a more complex situation. For example, Vermeulen et al. find many sources with substantial red and blue shifts, suggesting that atomic gas may be flowing out or falling in, interacting with the jets, or rotating around the nucleus.

Although many recent HI absorption studies have been based on samples of CSS and GPS objects, Morganti et al. (2001) observed extended radio galaxies from the 2-Jy sample of Wall & Peacock (1985), finding the following trends. HI absorption was detected in only 1 of the 10 FRI radio galaxies observed. For FRII radio galaxies, they detected HI absorption in 3 of 4 NLRGs, while absorption was not detected in any of 4 BLRGs. Although this is largely consistent with the predictions of the unified scheme (see van Ojik et al. 1997; Pihlström et al. 2003), the HI is blueshifted from the systemic velocity in 2 of the 3 NLRGs, suggesting that attributing the absorption to just a torus may be too simplistic.

In order to extend these HI investigations to a larger number of GPS and CSS objects, especially those that

Table 3. Observational details and results of the GMRT search for associated HI absorption.

Source name (1)	Date (2)	Obs. freq MHz (3)	BW MHz (4)	t_{int} hr (5)	Beam "×" ° (6)	Peak flux Jy/b (7)	σ mJy/b/ch (8)	$\sigma_{\text{FA}}^{\text{HI}}$ 10^{-3} (9)	FA _{max} (10)	W _{50%} km s ⁻¹ (11)	N(HI) 10^{20} cm ⁻² (12)
J0031–2652	2003 Dec	1065.570	4	3.5	3.9×2.8 19	0.55	1.8	<3.27	–	–	<1.90
J0040–2043	2003 Dec	1301.930	4	2.5	4.2×3.0 3	0.40	0.6	<1.50	–	–	<0.87
J0137+3309*	–	–	4	–	–	20.19	20	<1.00	–	–	<0.06
J0251+4315	2003 Jul	614.894	2	1.0	13.2×6.9 4	0.80	3.6	<4.50	–	–	<2.61
J0255–2153	2003 Dec	1276.425	4	3.0	3.1×2.5 30	0.44	2.8	<6.36	–	–	<3.69
J0347–2900	2003 Dec	1243.461	4	3.0	6.6×2.5 43	2.21	1.6	<0.72	–	–	<0.42
J1148+5924	2003 Jun	1405.299	4	1.5	4.9×2.8 34	0.62	0.6	<0.97	0.034	157	9.66±3.24
J1516+0015	2003 Dec	1350.196	4	3.5	5.1×4.9 59	0.68	0.6	<0.82	–	–	<0.51
J1521+0430	2003 Jul	618.644	2	1.3	29.3×8.0 43	4.34	4.8	<1.11	–	–	<0.64
						0.41					
J1604–2223	2003 Jul	1244.878	4	2.3	6.4×3.1 35	0.72	4.1	<5.69	–	–	<3.30
J2058+0542	2003 Jul	596.558	2	2.0	9.5×6.2 172	2.04	5.0	<2.45	–	–	<1.42
J2325+4346	2003 Jan	1240.529	8	3.2	3.0×1.9 56	0.48	0.7	<1.45	–	–	<0.84

Col. 1: source name; col. 2: year and month of observations; col. 3: redshifted 21-cm frequency; col. 4: baseband bandwidth (BW); col. 5: observing time in hr (excluding calibration overheads); cols. 6 & 7: restoring beam and peak brightness in Jy/beam for the continuum image made using line-free channels; col. 8: rms noise in the spectrum in units of mJy/beam/channel; col. 9: 1- σ noise for the HI fractional absorption; cols. 10 & 11: peak optical depth and FWHM for the absorption components derived directly from the spectra, and col. 12: HI column density in units of 10^{20} cm⁻², assuming T_s=100 K; upper limits are 3 σ values, and assume $\Delta v=100$ km s⁻¹ and $f_c=1.0$. The values of noise and peak optical depth have been estimated from the unsmoothed spectra except for J1148+5924 where the values have been estimated from the spectrum shown in Fig. 10.

* See text and Table 4 for details of the observations of J0137+3309 (3C48).

are of lower luminosity or more distant, and also towards larger sources, we have begun a program using the Arecibo 305-m telescope and the Giant Metrewave Radio Telescope (GMRT). In addition to HI, at Arecibo we have attempted to detect the OH radical which has so far received little attention in this context. In this paper we present the results of the first phase of our study and examine the dependence of HI column density on projected linear size, redshift, luminosity and host galaxy type by combining our results with those available in the literature. The observations are described in Section 2, while the results, with notes on individual sources, are presented in Section 3. In Section 4, we combine our results with those of similar HI searches and discuss the statistical trends in gas properties with respect to radio-source characteristics and redshift. The results are summarized in Section 5.

2 OBSERVATIONS

2.1 The observed sample

The principal targets of the Arecibo and GMRT observations were CSS and GPS sources whose redshifted 21-cm HI lines lie in the observing bands of these telescopes. In total, we observed 17 GPS and CSS sources with redshifts of $z \lesssim 1.4$. We also observed 7 large radio galaxies (LRGs; sizes $\gtrsim 15$ kpc), and 3 compact flat-spectrum (CFS) objects ($\alpha \lesssim 0.5$ and sizes $\lesssim 15$ kpc). At Arecibo, data were also recorded for the OH main-lines in an attempt to detect these in either emission or absorption. The sources and some of their properties are listed in Table 1. They form a heteroge-

neous set having been selected from a number of samples rather than a single well-defined complete sample. Possible selection effects arising from this are discussed later.

2.2 Arecibo observations and data reduction

The 15 radio sources observed at Arecibo consist of both GPS and CSS objects, and large FRI and FRII sources. The 7 CSS and GPS sources that formed the basic Arecibo sample were selected from well-defined samples of such objects (Fanti et al. 1990; Sanghera et al. 1995, and references therein) and a sample of compact symmetric objects (Taylor, Readhead & Pearson 1996). They have angular sizes of $\lesssim 1''$, with L-band flux densities in the range 0.3–5.4 Jy, and $z \lesssim 0.3$. Seven LRGs and one CFS object, all within the same flux density and redshift ranges, were added to fill gaps in the observing schedule. Six of the LRGs were chosen from the 3C sample. In addition to the HI observations, we made use of the versatility of the Arecibo spectrometer to simultaneously search for OH in all objects. Sadly, a number had their OH spectra corrupted by radio frequency interference (RFI). See Table 2 for the observing log.

The Arecibo feed platform and its support cables cause blockage to the incoming wave-front that is focussed on the telescope feed, and also scatter significant amounts of radiation from directions outside of the telescope main beam. The standing-wave pattern resulting from multipath scattering adds baseline ripples to a line spectrum. For standard Arecibo spectral-line observations of sources emitting little continuum radiation, such effects are minimized via a variant of the position-switching technique. However, when the target emits significant continuum radiation, the standing-wave

Table 4. Log for the GMRT observations of J0137+3309 (3C48).

Obs. run	Date	t_{int}^* hr	Obs. freq. MHz
1	2003 Oct 11	3.0	1039.8
2	2003 Dec 10	5.0	1040.6
3	2004 Aug 24	7.0	1037.7
4	2004 Aug 25	6.0	1037.7

* Integration time includes calibration overheads.

pattern due to the continuum emission from the target itself is not cancelled by subtracting the position-switched OFF from the ON, and a standing-wave residual remains whose amplitude is proportional to the source intensity. Briggs, Sorar & Taramopoulos (1993) extended the basic position switching method such as to minimize the effect of these residual standing waves. To achieve this, another strong continuum source (of different redshift) is also observed via position switching. Ghosh & Salter (2002) explored this “Double Position-Switching” (DPS) approach at Arecibo for sources having significant continuum emission and found it to be very effective in providing flat spectral baselines. We therefore adopted DPS for the present Arecibo observations of our sample, all of which emit significant continuum radiation.

The present observations recorded the orthogonal linear polarizations of both the λ 21-cm HI line, and the λ 18-cm OH main-lines. For all sources except J0119+3210 (see below), a bandwidth of 12.5 MHz was processed into 2048 channels, with data acquisition using 9-level quantization. The typical flux-density ratio for the DPS source pairs was 2:1. Weighted averages of the data for individual DPS cycles yielded the final spectra, which were Hanning smoothed. HI absorption was detected in five of the targets (J0119+3210, J1124+1919, J1347+1217, J1407+2827 and J2316+0405), and emission in a sixth (J0301+3512). Neither OH emission nor absorption was detected for any source. The rms noises on the HI and OH spectra of fractional absorption for a given (often smoothed) velocity resolution are listed in Tables 2 and 13. The peak fractional absorptions, integrated column densities and full-width half maxima for the five sources with detected HI absorption are given in Table 2.

2.3 GMRT observations and data reduction

Of the 12 radio sources observed with GMRT to search for associated HI absorption, 9 were selected from the sample of Snellen et al. (2002) and the Molonglo Reference Catalogue (MRC; Large et al. 1981; Kapahi et al. 1998a,b). Of the remaining three, two are the CSS objects J0137+3309 (3C48) and J2325+4346, and the third is the flat-spectrum source J1148+5924 (NGC3894). The angular size of each source is less than the spatial resolution of the observations.

HI absorption profiles for CSS sources exhibit a variety of shapes and can be as broad as several 100 km s^{-1} . Further, the profiles are often either blue- or red-shifted by a few 100 km s^{-1} with respect to the systemic velocity derived from the optical emission lines. To account for these factors, we used a baseband bandwidth (BB BW) of 8 MHz in our first observing run. However, we soon realised that

such broad bandwidths are both more difficult to calibrate, and susceptible to RFI. Thus for subsequent runs we used a BB BW of 4 MHz for observations at L-band, which has linearly-polarized feeds, and 2 MHz for those in the 610-MHz band, which has circularly-polarized feeds. This also gave the option of using the 6-MHz IF filter which helped minimise the effects of RFI. The GMRT FX correlator splits the BB BW into 128 frequency channels. The above choice of BB BWs thus implies a velocity resolution of $\sim 7 \text{ km s}^{-1}$, with a total typical velocity coverage of $\sim 1000 \text{ km s}^{-1}$, narrower than that of Vermeulen et al. (2003) by a factor of ~ 2 . Details of the GMRT observations are given in Table 3. GMRT calibration requires observations of standard flux density and phase calibrators. In all our observations, except for 3C48, the phase calibrator was observed approximately every 30 min. For bandpass calibration, a flux density calibrator (3C48, 3C147 or 3C286) was observed every 2–3 hr.

The CSS quasar J0137+3309 (3C48) was observed on a number of occasions (see Table 4) to search for HI absorption at $z_{abs}=0.3654$, the redshift at which Gupta, Sri-anand & Saikia (2005) detect outflowing material in the UV, and $z=0.3695$ and 0.3700, the emission-line redshifts from CO and optical observations respectively (cf. Gupta et al. 2005). The corresponding redshifted frequencies for 21-cm HI absorption lie in the 1060-MHz sub-band of GMRT. RFI at these frequencies not only makes the unambiguous detection of absorption and emission lines difficult, but also affects bandpass stability, thereby reducing the spectral dynamic range. Although a BB BW of 8 MHz was needed to cover the required redshifted frequencies, we chose to use a BB BW of 4 MHz and move this in frequency for the different observing sessions. Since 3C48 is itself a standard calibrator, it was not required to observe a separate flux density or phase calibrator. However, the high flux density of 3C48 ($\sim 20 \text{ Jy}$ at 1060 MHz) demands observing an equally strong bandpass calibrator, and for similar durations. We planned our observations such that 3C48 and 3C147 were observable at the same time. In all observing runs on 3C48, we observed it and 3C147 with a duty cycle of about 30 min. A log of the 3C48 observations is presented in Table 4. The integration time in column 3 includes the observing time for 3C147.

The NRAO AIPS package was used for the GMRT data reduction. In general, the data of the flux density calibrator, phase calibrator and source were examined at various stages for bad antennas, baselines and time ranges. In particular, the AIPS task SPFLG was invaluable for identifying data affected by RFI. Such data were then flagged out. The complex gains determined from the final cleaned data on the flux density, bandpass, and phase calibrators were used to calibrate the observed visibilities of each program source. A continuum image of a source was then made via the task IMAGR using data averaged over 10–15 line-free channels on both sides of the line. This image was then self-calibrated until a satisfactory map was obtained. This was not difficult as most fields are dominated by a strong point source at the phase centre. This continuum image was then Fourier transformed and subtracted from the visibility data cube using the task UVSUB. The continuum-subtracted data cube was then imaged (without cleaning) for all 128 channels to obtain a final image cube. The spectrum was obtained by taking a cut across the cube at the pixel corresponding to the source location. If necessary, a smooth low-order (usu-

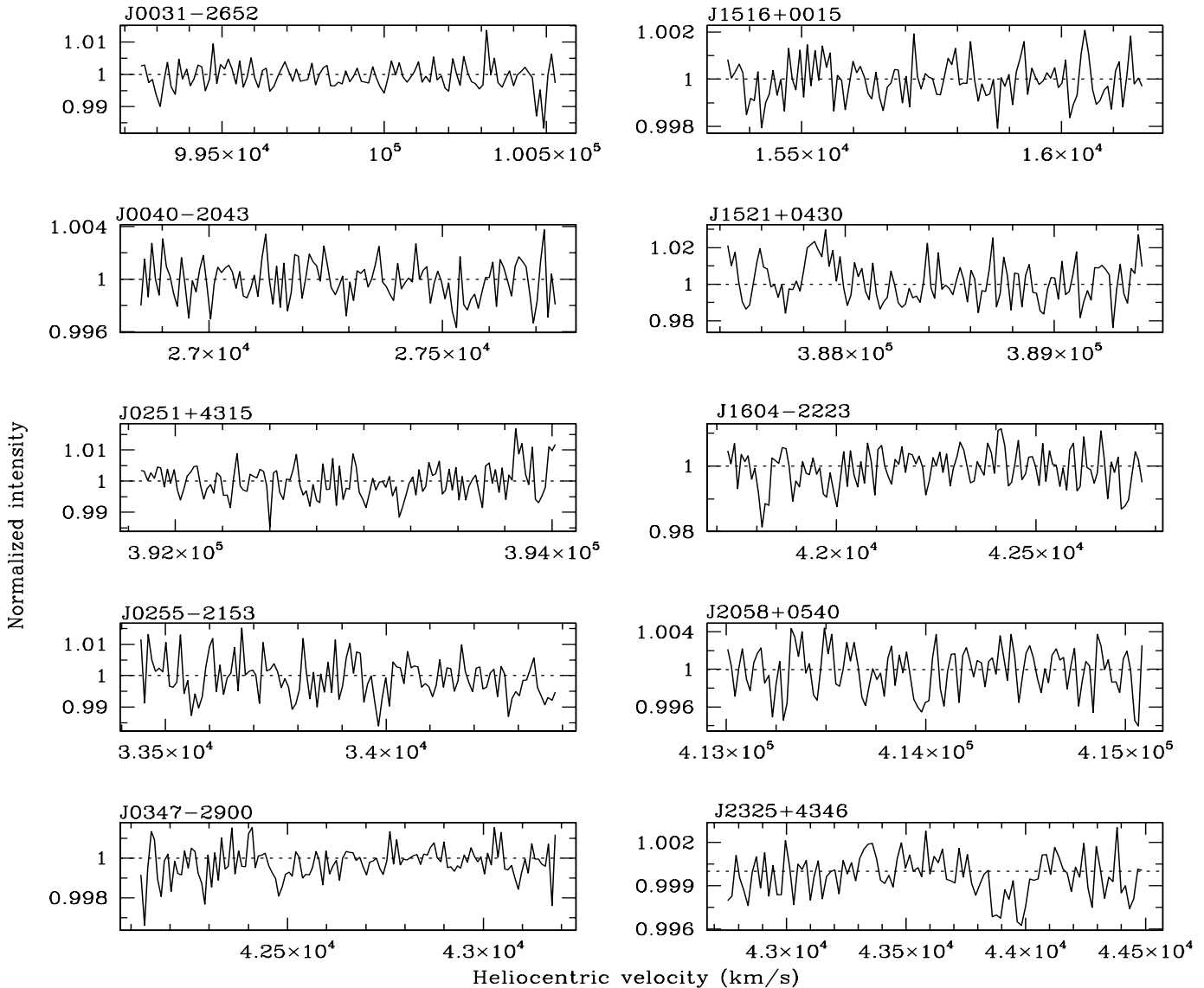


Figure 1. GMRT spectra for non-detections. The y-axis shows the normalized intensity while the x-axis shows the heliocentric velocity in km s^{-1} .

ally order one) cubic spline was fitted to take out residual bandpass effects or continuum subtraction errors. The spectra were then corrected to the heliocentric standard of rest.

3 OBSERVATIONAL RESULTS

3.1 HI observations

From our search for HI absorption towards 27 radio sources (Table 1), we made one new detection (3C258) and confirmed 5 previously reported HI absorption systems. In the case of NGC 1167, we have confirmed the double-horn shaped HI emission profile associated with the host E-S0 galaxy, which was reported by Wegner, Haynes & Giovanelli (1993). Of the remaining 20 sources, there was no useful data

for J1643+1715 (3C346), we have not been able to verify the detection towards J0901+2901 (3C213.1) by Vermeulen et al. (2003) while for J2250+1419 (4C+14.82) our Arecibo spectrum provides significant improvement over the limit of Vermeulen et al. For J0137+3309 (3C48), we do not detect any absorption line in our deeper spectrum although a preliminary detection was reported by Pihlström (2001). The $\text{N}(\text{HI})$ upper limits on the remaining 16 sources are new.

The absorption lines detected were fitted with multiple Gaussians to determine the peak optical depth (τ_p) and FWHM (Δv ; in km s^{-1}) of spectral components. The parameters derived from the fits are considered in detail in Section 3.3. HI column densities were determined using the

relations

$$\begin{aligned} N(\text{HI}) &= 1.835 \times 10^{18} \frac{T_s \int \tau(v) dv}{f_c} \text{ cm}^{-2} \\ &= 1.93 \times 10^{18} \frac{T_s \tau_p \Delta v}{f_c} \text{ cm}^{-2} \end{aligned} \quad (1)$$

where T_s and f_c are the spin temperature (in K) and the fraction of the background emission covered by the absorber respectively. We have assumed $T_s=100$ K and $f_c=1.0$. For non-detections, the upper limits on the HI column densities were calculated by replacing the τ_p in the above equation by 3σ upper limits to the peak optical depths estimated from the rms in the spectra, and assuming $\Delta v=100$ km s $^{-1}$. Measured HI column densities, and limits estimated as above, for the Arecibo sources are contained in Table 2. The rms noises in the GMRT spectra, and constraints on the peak HI optical depths and column densities towards the GMRT sources, are presented in the last 3 columns of Table 3; the spectra for GMRT non-detections are shown in Fig. 1. One of the deepest Arecibo non-detections is shown in Fig. 8. The spectra for all detections are presented in Section 3.3.

3.2 OH observations

The 15 sources observed with the Arecibo telescope were also searched for OH main-line emission and/or absorption. The observations were unaffected by RFI for 9 objects, but none revealed either emission or absorption. Interpretation of these results is presented in Section 4.7.

3.3 Notes on individual sources

J0034+3025: This galaxy was not detected in either HI or OH. For OH, the segment of the observed spectrum between 1420.14 and 1420.72 MHz was corrupted by the presence of Galactic HI.

J0040–2043: This source was listed earlier as unresolved with an LAS $<5''$ (Kapahi et al. 1998a). Our GMRT image (Fig. 2) at \sim 1300 MHz shows an unresolved component of LAS $\lesssim2.4''$ and diffuse emission extending up to at least $15''$. From our map, the peak brightness and integrated flux density are 0.40 Jy/beam and 0.61 Jy respectively.

J0119+3210 (4C+31.04): The mas-scale radio images of this source show two lobes separated by \sim 80 mas along a position angle (PA) of \sim 110° (Cotton et al. 1995). A faint flat-spectrum component was identified by Giovannini et al. (2001) as the core which, with the absence of any jet-like structures, led them to suggest that the source is oriented close to the plane of the sky, with an angle of inclination to the line of sight, $\theta \geq 75^\circ$.

HI absorption was first detected in this object by van Gorkom et al. (1989) and Mirabel (1990), who discovered that the source also displayed a high velocity component relative to the systemic velocity of the galaxy. The full HI spectrum was subsequently studied in detail via VLBI observations by Conway (1999). He interpreted the distribution of HI opacity as due to an HI disk whose axis is aligned with the jet axis, i.e. close to the plane of the sky. The disk covers the eastern lobe completely, but only the inner part of the western lobe. The high velocity component then arises from small clouds evaporating off the inner edge of the disk. The

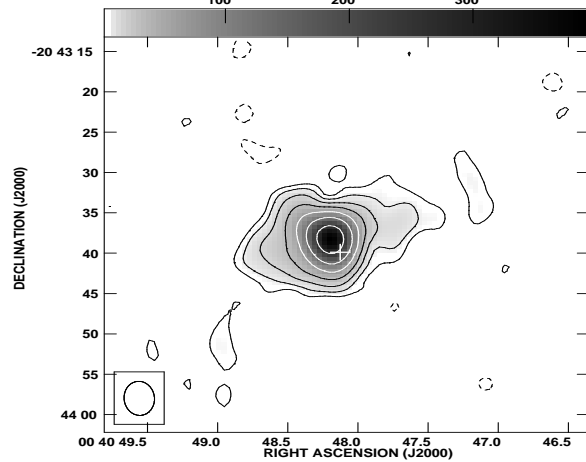


Figure 2. GMRT image of J0040–2043 at 1300 MHz with an rms noise of 1.4 mJy/beam. The contour levels are $4 \times (-1, 1, 2, 4, 8, 16, 32 \text{ and } 64)$ mJy/beam. The restoring beam (see Table 3) is shown as an ellipse and the position of the optical host galaxy (McCarthy et al. 1996) is marked with a cross.

existence of this disk is further supported by an S-shaped dust lane with an inner PA of $\sim 25^\circ$ as seen in HST images (Capetti et al. 2000).

Sadly, the OH main lines are redshifted near to the frequency of GPS-L1 transmissions making them unobservable. Consequently, we decided to observe the HI spectrum at Arecibo with both high and low resolution, using total bandwidths of 3.125 and 25.0 MHz, each with 2048 spectral channels. The high resolution spectrum (Fig. 3: top) was used to fit Gaussian components to the main and high-velocity feature separately (Fig. 4), while the low resolution spectrum (Fig. 3: bottom) was used to search for any further weak absorption components separated in velocity from the others. The number of Gaussians fitted here, (and for other sources), was the minimum needed to reduce the post-fit residuals to noise.

For the high resolution spectrum, the main component is fitted well by four Gaussians, while the high-velocity feature requires only two. These are summarized in Table 5. The low-resolution spectrum shows only a single possible absorption feature separated from the stronger features; a small dip of optical depth ~ 0.001 at heliocentric velocity ~ 18530 km s $^{-1}$. This appears at the 3.5σ level on a smoothed version of Fig. 3: bottom. Confirmation would be required before its reality could be claimed with confidence.

J0137+3309 (3C48): This enigmatic CSS quasar has a complex radio morphology which has been interpreted as being due to the interaction of the jet with the host galaxy's interstellar medium (Wilkinson et al. 1991). The jet-cloud interaction scenario is further supported by the properties of blue-shifted gas detected in forbidden emission lines (Chatzicristou, Vanderriest & Jaffe 1999). Recently, Gupta et al. (2005) reported the detection of a $z_{abs}=0.3654$ associated absorption-line system in an UV spectrum. A tentative detection of HI absorption towards 3C48 was reported by Pihlström (2001) with a peak optical depth of 0.001

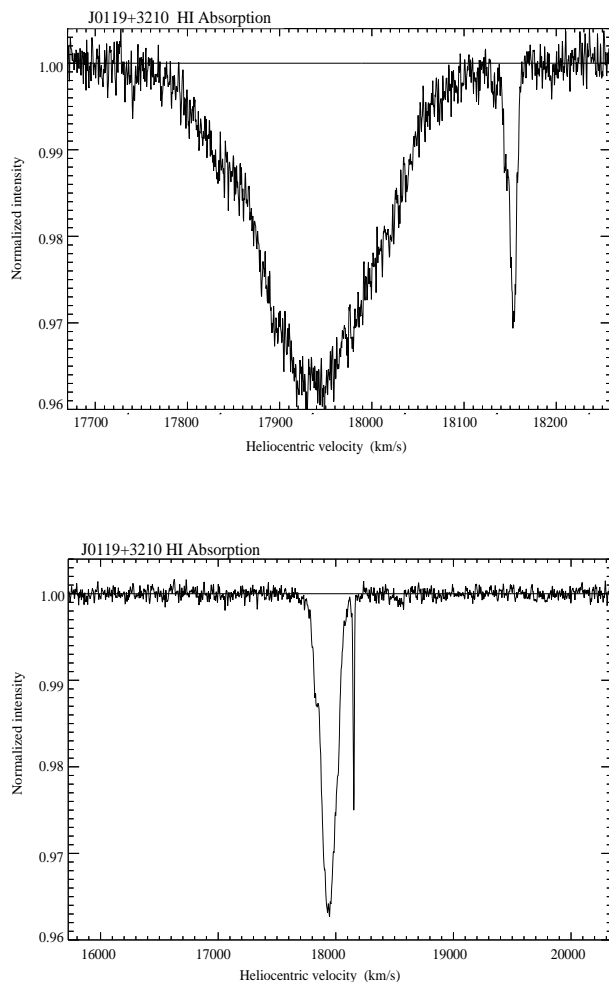


Figure 3. HI absorption spectra of J0119+3210 (4C+31.04). Top: The high-resolution spectrum. Bottom: The low-resolution spectrum with the wider wavelength coverage.

Table 5. Multiple-Gaussian fits to the broad and narrow absorption features towards the radio source J0119+3210 (4C+31.04).

Id. no.	v_{hel} km s^{-1}	FWHM km s^{-1}	Frac. abs.	$N(\text{HI})$ 10^{20} cm^{-2}
Broad				
1	17858.2(3.3)	108.2(2.9)	0.0121(0.0001)	2.53(0.07)
2	17891.2(0.7)	26.1(2.2)	0.0045(0.0001)	0.23(0.02)
3	17930.5(0.4)	78.3(0.7)	0.0276(0.0003)	4.17(0.06)
4	17994.4(1.1)	93.7(0.9)	0.0211(0.0001)	3.81(0.04)
Narrow				
1	18145.3(0.06)	7.19(0.09)	0.0100(0.0002)	0.14(0.01)
2	18153.7(0.01)	7.78(0.01)	0.0285(0.0002)	0.43(0.01)

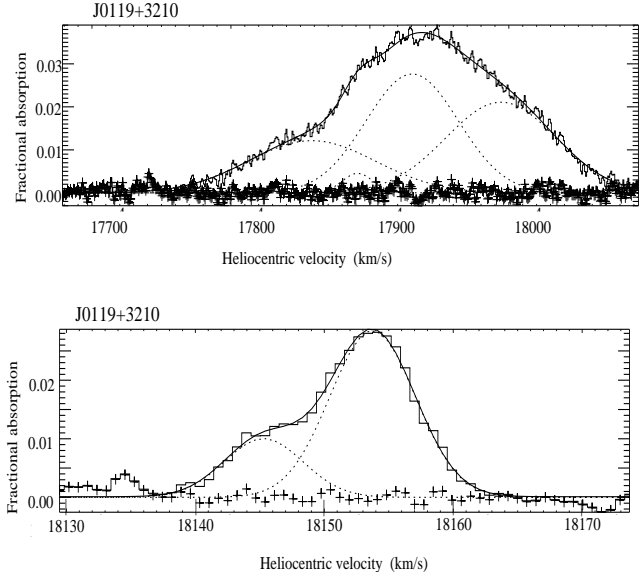


Figure 4. The Gaussian fits to the HI absorption spectrum of J0119+3210 (4C+31.04). The high-resolution spectrum (histogram) with a velocity resolution of 0.72 km s^{-1} is plotted along with the four-component Gaussian fit to the broad component (top) and two-component Gaussian fit to the narrow high-velocity component (bottom). The individual Gaussians are shown dotted, and their sum as a solid line. The residuals, following subtraction of the Gaussians, are shown as crosses.

and FWHM of 100 km s^{-1} . Our deep GMRT observations (Fig. 5) fail to reveal detectable HI absorption at either the systemic redshift of 3C48 or the redshift corresponding to the gas responsible for the UV absorption lines. For the flux density of 20.3 Jy determined from our observations and assuming $f_c=1.0$, we obtain a 3σ upper limit on optical depth in the range of 0.001 to 0.003 from the unsmoothed spectra shown in Fig. 5.

J0251+4315: The source structure in the VLBA images at 2.3 and 8 GHz show two prominent components, but appear to be better described by a multi-component structure (Fey & Charlot 2000). We detect no significant HI absorption feature associated with this GPS quasar in our GMRT spectrum. The quasar is part of a quasar-galaxy pair with the foreground galaxy G0248+430 ($z=0.052$) located at a distance of $\sim 15''$ along a PA of 105° (Sargent & Steidel 1990). The GMRT 616-MHz image (Fig. 6) also shows continuum emission from the galaxy which has a flux density of $\sim 25 \text{ mJy}$ at this frequency.

J0301+3512 (NGC1167): The Arecibo HI spectrum of this low redshift, E-S0, galaxy, which has a somewhat complex radio structure (Sanghera et al. 1995), shows no recognizable absorption. However, an emission spectrum typical of a spiral galaxy is seen (Fig. 7), where the spectrum has been normalized into Jy beam^{-1} , as is appropriate for line emission. The parameters derived from the spectrum are a HI line flux density of $6.22 \pm 0.4(1\sigma) \text{ Jy km s}^{-1}$, a heliocentric radial velocity of 4965 km s^{-1} , and line widths of 504 and 511 km s^{-1} at 50% of the mean and 20% of the peak signal intensity respectively. These values agree reasonably with those given by Wegner et al. (1993). As implied by the entry for J0301+3512 in Table 2 of Wegner et al., the

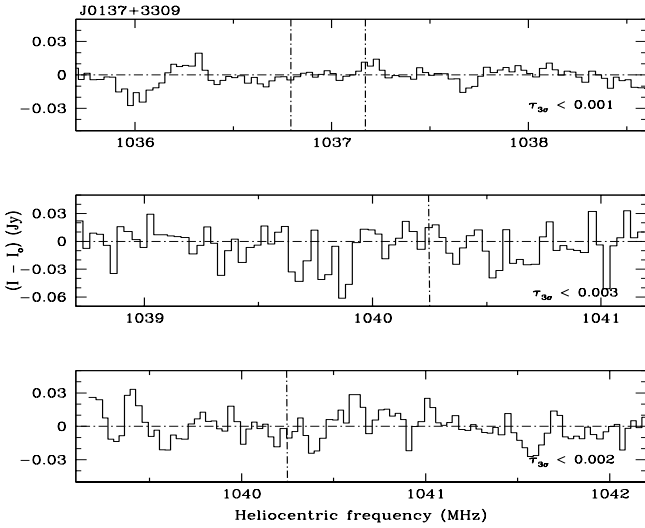


Figure 5. GMRT spectra of J0137+3309 (3C48) covering the redshifted 21-cm frequency (marked by vertical lines) corresponding to $z_{em}=0.3700$ from the optical emission lines, $z_{em}=0.3695$ from the CO emission spectrum (upper panel) and $z_{abs}=0.3654$ corresponding to the blue-shifted absorbing material (middle and lower panels) detected in the UV by Gupta et al. (2005).

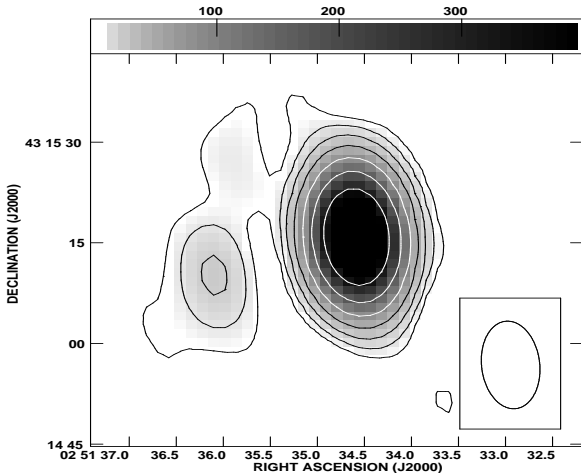


Figure 6. GMRT image of J0251+4315 at 616 MHz with an rms noise of 1.6 mJy/beam. The contour levels are $5 \times (-2, -1, 1, 2, 4, 8, 16, 32 \text{ and } 64) \text{ mJy/beam}$. The restoring beam (see Table 3) is shown as an ellipse. The eastern feature is the foreground galaxy G0248+430.

HI emission from this galaxy is expected to be significantly resolved by the Arecibo beam at 21-cm. Earlier HI observations have been reported by Heckman et al. (1983) and Chamaraux, Balkowski & Fontanelli (1987) who suggested that the HI gas distribution may be influenced by tidal interactions with two disk galaxy companions.

J0513+0157 (4C+01.13): Perlman et al. (1998) classified the parent optical object as a BL Lac on the basis of Ca II break strength and lack of emission lines. However, due to

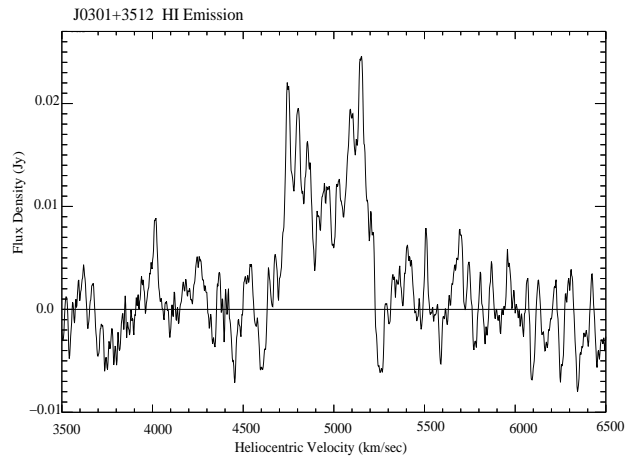


Figure 7. The double-horn shaped HI emission profile of the E-SO galaxy NGC 1167 (J0301+3512).

the low signal-to-noise ratio of the spectrum blueward of the Ca II break, its classification as a radio galaxy cannot be ruled out. The OH observations for this source were corrupted by extensive RFI across the band. At the time of observations, the best available redshift for this source was $z = 0.084$. However, Rines et al. (2003) have since measured an improved value of $z = 0.08808 \pm 0.00014$, which would place the HI line towards the edge of the present spectrum. Nevertheless, there is still sufficient baseline to say with confidence that no HI absorption is seen for the source at the 3σ level for the parameters given in Table 2.

J0725-0054: This narrow-line radio galaxy, which has an asymmetric radio structure with a knotty jet extending for $\gtrsim 30$ mas along $\text{PA} \sim -24^\circ$ (Fey & Charlton 1997; Bondi et al. 1996), was observed with the then best available redshift of $z = 0.128$. An improved value of $z = 0.1273 \pm 0.0001$ has since been measured by Eracleous & Halpern (2004). RFI is present over part of the Arecibo HI spectrum, with no HI absorption being detected in the uninterfered spectral region corresponding to $0.1247 < z < 0.1291$. The OH spectrum is RFI-free, and again neither emission nor absorption is seen.

J0805+2409 (3C192): This FRII source has an X-shaped structure (Baum et al. 1988). It is marginally resolved by the Arecibo beam at 1340 MHz, its measured flux density representing $\sim 84\%$ of the total. No HI absorption was detected, while the OH spectrum was destroyed by RFI from GPS-L1 transmissions.

J0822+0557 (3C198): The OH spectrum for this classical double-lobed FRII radio galaxy (Fomalont 1971), was destroyed by RFI. With its large angular diameter, it is heavily resolved by the Arecibo beam at 1315 MHz, the measured flux density representing only $\sim 63\%$ of the total. No HI absorption was detected.

J0901+2901 (3C213.1): This galaxy has emission that extends up to $\sim 40''$ in addition to a more compact double-lobed structure (Akujor et al. 1991). A detection of HI absorption in it was recently reported by Vermeulen et al. (2003). The optical depth that they measured was $\tau = 0.0005$, the lowest value detected in their survey by a factor of ~ 3 . Although this source provided one of the lowest rms optical depth limits among our Arecibo observa-

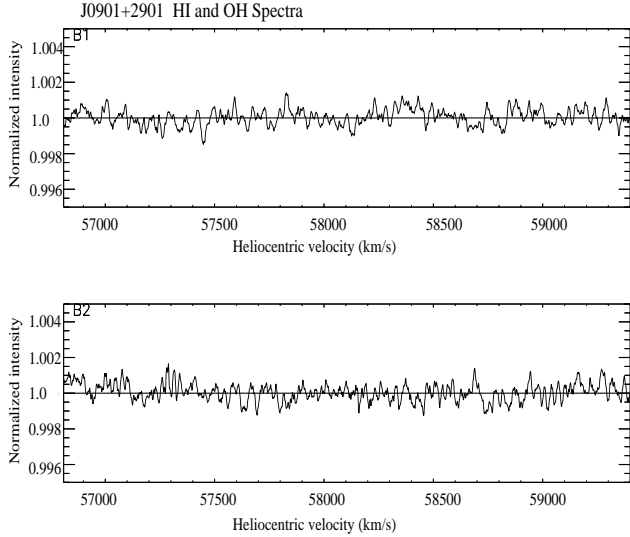


Figure 8. HI and OH spectra for J0901+2901 (3C213.1); the y-axis is the spectral intensity normalized by the source flux density, while the x-axis is the heliocentric velocity in km s^{-1} . Top: the HI spectrum with a velocity resolution of 16.5 km s^{-1} ; bottom: the OH spectrum with a velocity resolution of 14.1 km s^{-1} .

Table 6. Multiple-Gaussian fit to the HI absorption spectrum of J1124+1919 (3C258).

Id. no.	v_{hel} km s^{-1}	FWHM km s^{-1}	Frac. abs.	$N(\text{HI})$ 10^{20} cm^{-2}
1	49500.1(0.05)	9.69(0.04)	0.0532(0.0013)	1.00(0.03)
2	49508.3(0.09)	7.64(0.28)	0.0304(0.0011)	0.45(0.02)
3	49514.2(0.07)	5.71(0.14)	0.0226(0.0026)	0.25(0.03)
4	49525.1(0.03)	12.50(0.01)	0.0968(0.0002)	2.34(0.01)
5	49546.1(0.06)	11.73(0.11)	0.0290(0.0002)	0.66(0.01)
6	49553.4(0.20)	3.60(0.49)	0.0070(0.0008)	0.05(0.01)
7	49564.2(0.38)	8.23(0.78)	0.0056(0.0002)	0.09(0.01)

tions (Fig. 8: top), this is still not deep enough to verify the detection of Vermeulen et al. The Arecibo OH spectrum (Fig. 8: bottom) shows neither emission nor absorption to a similar optical depth limit as for HI. The spectra shown illustrate one of the deeper Arecibo non-detections.

J1124+1919 (3C258): Deep HI absorption (Fig. 9: left) was detected for the first time against the continuum emission from this radio galaxy. This emission is dominated by the CSS source but it is known to also have more extended emission (Strom et al. 1990; Sanghera et al. 1995). The FWHM of the line is at the narrow end when compared to values listed by Pihlström et al. (2003). Despite this, it shows considerable structure, and seven Gaussian components are needed to fit the spectrum satisfactorily (Fig. 9: right). These components are listed in Table 6.

The individual Gaussian components are narrow, with half-height widths lying between ~ 4 and 12 km s^{-1} . These narrow widths for the fitted components imply rather low upper limits on T_s values for the HI, the derived values lying in the range $T_s \lesssim 400 - 2000 \text{ K}$. Compared to other CSS HI-absorption systems, 3C258 exhibits an unusually complex

Table 7. Multiple-Gaussian fit to the HI absorption spectrum of J1148+5924 (NGC3894).

Id. no.	v_{hel} km s^{-1}	FWHM km s^{-1}	Frac. abs.	$N(\text{HI})$ 10^{20} cm^{-2}
1	3161(4)	44.53(6.50)	0.0061(0.0006)	0.52(0.09)
2	3223(2)	51.74(3.58)	0.0161(0.0046)	1.61(0.47)
3	3262(2)	61.44(17.44)	0.0181(0.0024)	2.15(0.67)
4	3300(2)	75.77(12.26)	0.0237(0.0039)	3.47(0.80)
5	3352(2)	41.04(2.88)	0.0207(0.0024)	1.64(0.22)
6	3396(5)	32.26(7.34)	0.0044(0.0008)	0.27(0.08)

spectrum, with the components having about an order of magnitude narrower velocity widths than for most, though not all, features in other CSS sources (Vermeulen et al. 2003; Pihlström et al. 2003). The possibility of the existence of weak, extended line wings, as suggested by Fig. 9: left, will have to await deeper integrations for confirmation.

Although detailed modelling of the HI gas seen in absorption in this galaxy will require VLBI imaging of the line and continuum emission, it is difficult to imagine that a single rotating disk/torus would produce such a complex absorption system. This may be a miniature version of 3C236, where jet-ISM interactions play the dominant role in shaping the structure/properties of the object. In fact, the signature of disturbance is perhaps already evident in its optical image. The HST image of 3C258 (de Vries et al. 1997) displays an arc-like structure of high surface brightness, with a larger, fainter tail extending to the northeast, roughly perpendicular to the bright central arc. The radio continuum image (Akujor et al. 1991) is at right angles to the central region and contains the entire VLBI-scale double-lobed structure (Sanghera et al. 1995). Neither OH absorption nor emission were detected against 3C258.

J1148+5924 (NGC3894): The galaxy NGC3894, classified as an E/S0, lies at a redshift of $z=0.01075$ (de Vaucouleurs et al. 1991). This is in agreement within the error of $\pm 30 \text{ km s}^{-1}$, with the redshift of $z=0.01068$ determined by Karachentsev (1980). Using multi-epoch VLBI observations, Taylor, Wrobel & Vermeulen (1998) suggest that the radio source is oriented well away from the line of sight ($\theta \sim 50^\circ$). Redshifted HI absorption has been detected towards both the approaching and receding jets by Peck & Taylor (1998). Our GMRT spectrum (Fig. 10) shows the HI absorption towards this radio source. A good fit to the absorption profile was obtained using six Gaussian components. The best-fit parameters are summarised in Table 7. Most of the absorption features are redshifted with respect to the systemic velocity ($\sim 3220 \text{ km s}^{-1}$) and could represent the large-scale circumnuclear disk, as well as clouds infalling towards the central engine (Peck & Taylor 1998).

J1347+1217 (4C+12.50): This CSS source is associated with a Seyfert-2 galaxy containing two nuclei separated by $2''$, which may be in the process of merging (Gilmore & Shaw 1986). Broad $\text{Pa}\alpha$ emission ($\Delta v_{\text{FWHM}} \approx 2600 \text{ km s}^{-1}$) suggests that it may contain a buried quasar (Veilleux, Sanders & Kim 1997). The radio structure is highly asymmetric and has a jet on VLBI scales (Xiang et al. 2002; Lister et al. 2003).

Mirabel (1989) detected broad HI absorption against

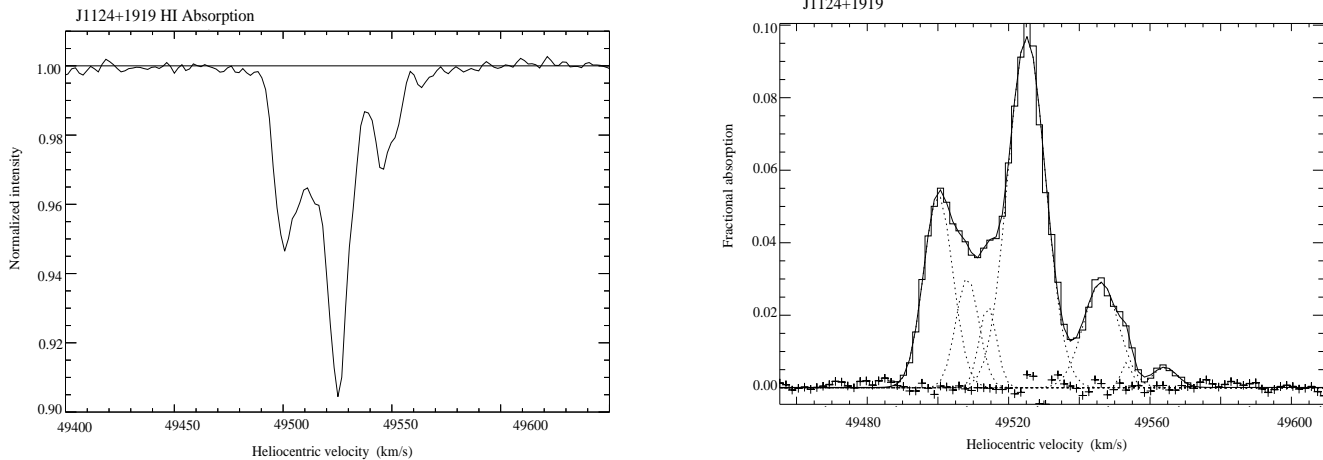


Figure 9. Left: The HI absorption spectrum for J1124+1919 (3C258) with a velocity resolution of 3.5 km s^{-1} . Right: The same spectrum plotted as a histogram, overlaid by the seven Gaussians fitted to the spectrum. The meanings of the different line types are as in Fig. 4.

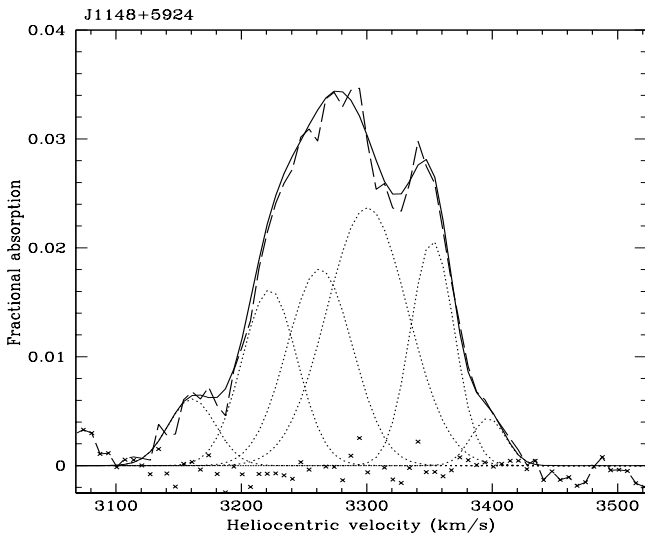


Figure 10. The HI absorption spectra (dashed line) for J1148+5924 (NGC3894) obtained with the GMRT. The spectrum has been smoothed using a 5 pixel wide boxcar filter. The six Gaussian components fitted to the absorption profile, the sum of these component fits and residuals are plotted as dotted and solid lines, and crosses respectively.

this radio galaxy, followed shortly afterwards by the detection (Mirabel, Sanders & Kazès 1989) of very broad CO($1 \rightarrow 0$) emission (see also Scoville et al. 2000). The HI spectrum of Mirabel (1989) showed a deep ‘core’ near the redshift of the galaxy, and apparent very broad wings covering a total velocity range of 950 km s^{-1} . Morganti et al. (2004) recently demonstrated that the line wings have an optical depth of $\lesssim 0.002$, and cover some 2000 km s^{-1} , extending especially to the blue. We are unable to add anything on these line wings, both because of sensitivity and the presence of RFI at 1370 MHz ($v \sim 35500 \text{ km s}^{-1}$). However, our spectrum has higher velocity resolution on the core than previously published examples, and is shown in Fig. 11:top. There is an indication of broadening of the redshifted side of the

Table 8. Multiple-Gaussian fit to the HI absorption spectrum of J1347+1217 (4C+12.50).

Id. no.	v_{hel} km s^{-1}	FWHM km s^{-1}	Frac. abs.	$N(\text{HI})$ 10^{20} cm^{-2}
1	36547.4(0.4)	129.9(0.7)	0.0107(0.0001)	2.68(0.03)
2	36611.9(0.8)	22.8(1.8)	0.0023(0.0001)	0.10(0.01)
3	36649(1.7)	23.5(3.9)	0.0018(0.0001)	0.08(0.01)

line core, and a smoothed version of the spectrum can be fitted well by three Gaussian components (see Fig 11:bottom), where the best-fit parameters are listed in Table 8.

A recently published redshift for this object by Holt, Tadhunter & Morganti (2003) gives $z = 0.12174 \pm 0.00002$ ($v = 36497 \pm 6 \text{ km s}^{-1}$). This is consistent with our broad core component #1 being associated with the nucleus of the galaxy.

From the OH spectrum for J1347+1217 neither emission nor absorption is detected. The source was included in the sample of Darling & Giovanelli (2002), for which they searched for OH megamaser emission at Arecibo. However, they were unable to provide a meaningful limit to such emission for this object due to the effects of standing waves. Dickey et al. (1990) reported a tentative detection of OH emission in this source of peak flux density $1.7 \pm 0.2 \text{ mJy}$, and a line width of $305 \pm 44 \text{ km s}^{-1}$. Smoothing our spectrum to a velocity resolution of 35 km s^{-1} , we can set an upper limit on the presence of 1667-MHz OH emission of 4.8 mJy (3σ). A deeper integration would be valuable.

J1407+2827 (Mrk668): This GPS object has an asymmetric double-lobed structure and is embedded in a galaxy with highly irregular isophotes, suggesting dynamical disturbance (Stanghellini et al. 1993, 2001). Broad, but weak, HI absorption was detected against this source by Vermeulen et al. (2003). We confirm this (Fig. 12), and find evidence of structure within the feature. The line is well fitted by three Gaussian components, the best-fit parameters being listed in Table 9.

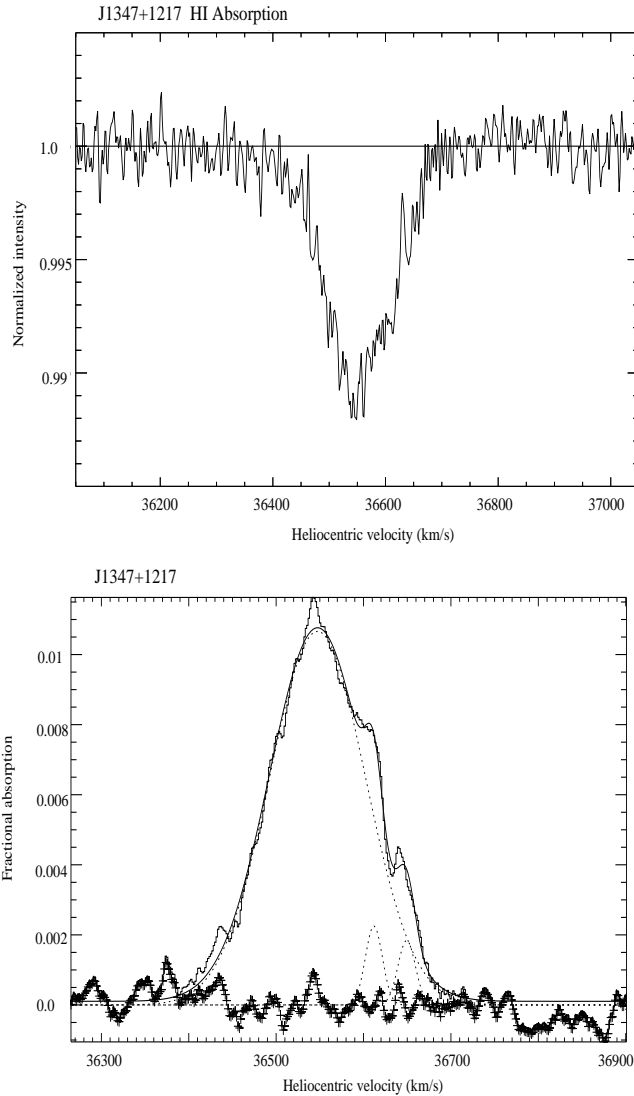


Figure 11. Top: The HI absorption spectrum towards the radio source J1347+1217 (4C+12.50) at a spectral resolution of 3.2 km s^{-1} . Bottom: The Gaussian fits to the components at a velocity resolution of 28.8 km s^{-1} . The line types are as in Fig. 4.

Table 9. Multiple-Gaussian fit to the HI absorption spectrum of J1407+2827 (Mrk668).

Id. no.	v_{hel} km s^{-1}	FWHM km s^{-1}	Frac. abs.	$N(\text{HI})$ 10^{20} cm^{-2}
1	22991(16)	71(23)	0.0019(0.0001)	0.26(0.08)
2	23097(7)	111(21)	0.0030(0.0001)	0.64(0.12)
3	23227(6)	90(11)	0.0030(0.0001)	0.52(0.07)

Recently published redshifts for this object are $z=0.07658\pm0.00013$ (Huchra et al. 1990) and $z=0.07681\pm0.00007$ (Eracleous & Halpern 2004). Our measured redshift for the fitted HI components of $z=0.07669(5)$, $0.07704(2)$ and $0.07748(2)$ suggest that the two stronger components are consistent with infall on to the

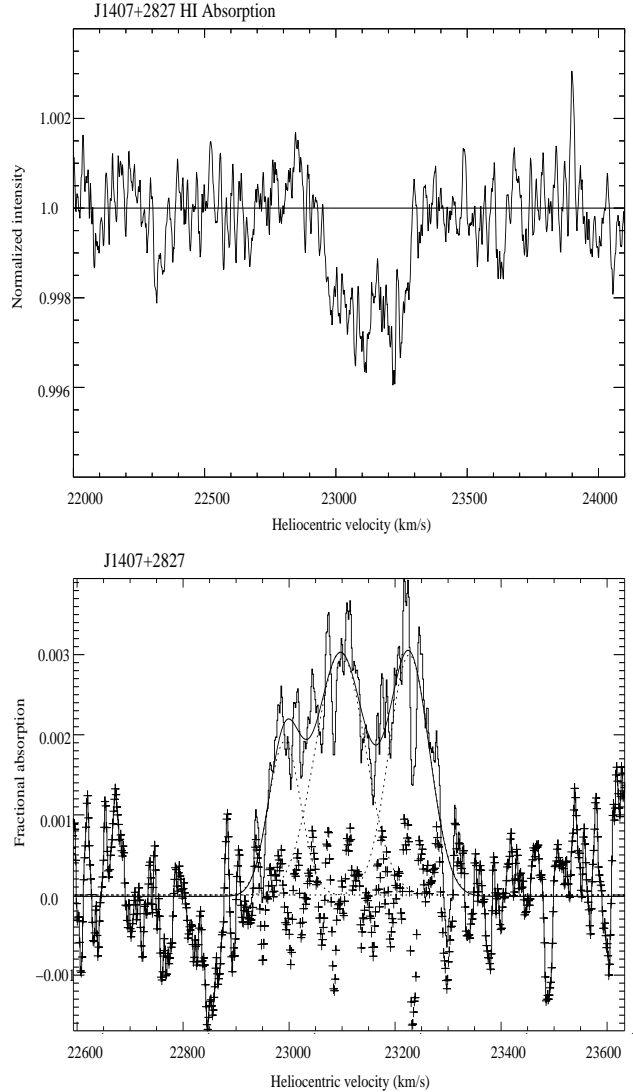


Figure 12. Top: The HI absorption spectrum towards the radio source J1407+2827 (Mrk668). Bottom: The three Gaussian components are overlaid on the spectrum. The line types are as in Fig. 4.

galactic nucleus. Unfortunately, the OH spectrum for this source was corrupted by extensive RFI.

J1521+0430 (4C+04.51): In addition to the compact VLBI-scale double of this GPS source, which is unresolved in our 619-MHz observations, there is a separate component towards the south-east at an angular distance of $\sim 1'$ (Fig. 13). Comparing this with the NVSS image yields a spectral index of ~ 0.7 between ~ 620 and 1400 MHz. It is unclear whether this component is related to our source, although $\sim 10\%$ of GPS sources are known to have radio emission beyond kpc scales (Stanghellini et al. 1990). A more sensitive low-frequency image is required to establish whether this feature is related to the GPS source.

J1643+1715 (3C346): The parent galaxy of 3C346 has a double nucleus, the compact, north-western component being coincident with the radio core (Dey & van Breugel 1994). The source has a one-sided radio jet extending for $\sim 2''$ (Cotton et al. 1995), and diffuse extended emission on

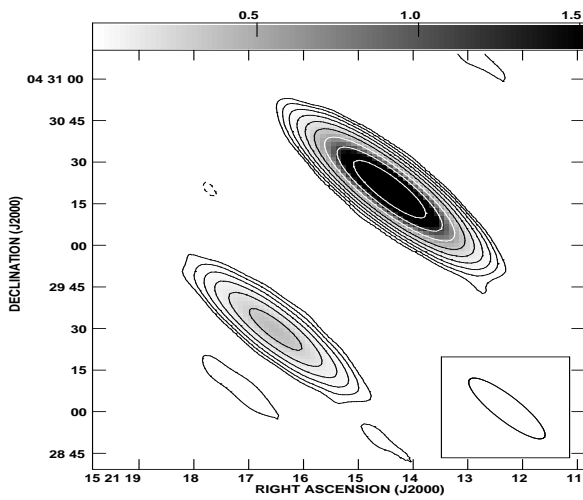


Figure 13. GMRT image of J1521+0430 (4C+04.51) at 619 MHz with an rms of 3 mJy/beam. The contour levels are $9 \times (-2, -1, 1, 2, 4, 8, 16, 32, 64, 128 \text{ and } 256)$ mJy/beam. The restoring beam (see Table 3) is shown as an ellipse.

Table 10. Multiple-Gaussian fit to the HI absorption spectrum of J2316+0405 (3C459).

Id. no.	v_{hel} km s^{-1}	FWHM km s^{-1}	Frac. abs.	$N(\text{HI})$ 10^{20} cm^{-2}
1	65510(27)	71(34)	0.0012(0.0001)	0.17(0.08)
2	65616(6)	121(11)	0.0034(0.0001)	0.80(0.08)
3	65809(31)	164(63)	0.0012(0.0001)	0.38(0.15)

a scale of $\sim 12''$ (Akujor et al. 1995). The one-sided jet suggests a small angle of inclination to the line of sight. The HI spectrum for this source were corrupted by the effects of GPS-L2 transmissions. However, the OH spectrum is good, but neither emission nor absorption is detected.

J2250+1419 (4C+14.82): This CSS quasar has an angular size of $0''.2$ (Spencer et al. 1989). It was observed with the spectra centered on the then-best redshift, $z = 0.237$. A value of $z = 0.23478(8)$ has recently been published by Eracleous & Halpern (2004). However, this update is small, and any absorptions near the revised redshift would still lie well within the present spectra. In practice, 4C+14.82 has no detected line of either HI or OH. The $N(\text{HI})$ limit obtained here is a significant improvement over the spectrum of Vermeulen et al. (2003).

J2316+0405 (3C459): This highly-asymmetric radio galaxy with a steep-spectrum core is associated with a galaxy that exhibits tidal tails and has a high infrared luminosity (Thomasson, Saikia & Muxlow 2003). HI absorption has been reported for 3C459 by Morganti et al. (2001) and Vermeulen et al. (2003). The Arecibo HI observations confirm the presence of this line, (see Fig. 14: top). Three Gaussian components fit the line well, the best-fit parameters being listed in Table 10, and shown in Fig. 14: bottom.

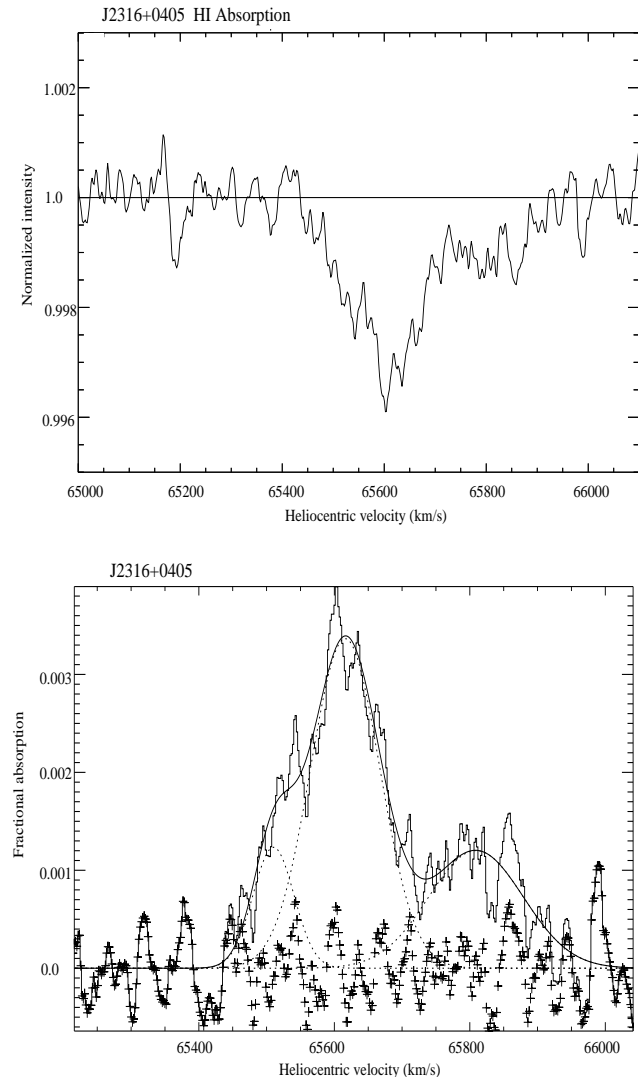


Figure 14. Top: The HI absorption spectrum for J2316+0405 (3C459). The velocity resolution is 17.2 km s^{-1} . Bottom: The same spectrum overlaid by the three Gaussians fitted to it. The line types are same as in Fig. 4.

A recently published redshift for this object by Eracleous & Halpern (2004) gives $z = 0.2201 \pm 0.0002$ ($v = 65984 \pm 60 \text{ km s}^{-1}$) from the average of 4 low-ionization lines. All three fitted HI components are significantly blue-shifted relative to this, consistent with outflow from the galactic nucleus.

The OH spectrum for J2316+0405 reveals neither emission nor absorption. Like J1347+1217, this source was also in the Arecibo sample of Darling & Giovanelli (2002), but again no meaningful limit to its OH emission was set by them due to the effects of standing waves.

4 DISCUSSION AND ANALYSES OF THE ‘FULL SAMPLE’

Of 27 radio sources observed with the Arecibo telescope and GMRT, we detect associated HI absorption towards 6

and HI emission for one other. Individual HI emission- and absorption-line systems have been discussed in detail in Section 3.3. The source sample we have used contains objects ranging from the very compact GPS, CSS and CFS sources (sub-kpc to a few kpc) to large radio sources (a few hundred kpc). Hence, these observations allow us to use radio continuum emission spread over a variety of scales as background sources to search for associated neutral gas. In this Section, we combine our results with those of similar HI searches and discuss the trends in gas properties with respect to radio-source characteristics and redshift.

4.1 The ‘full sample’

In order to have a large enough sample to investigate these trends, we consider the associated HI -absorption searches reported by van Gorkom et al. (1989), Peck et al. (2000), Morganti et al. (2001), Pihlström (2001), Vermeulen et al. (2003) and Pihlström et al. (2003). These used a variety of instruments and set-ups, each having different bandwidths, spectral and spatial resolutions. In the pioneering study of van Gorkom et al. (1989) a total bandwidth of 6.25 MHz ($\sim 1300 \text{ km s}^{-1}$) was used. It detected HI absorption in 4 of 29 galaxies, all 4 being redshifted relative to the systemic velocity. Vermeulen et al. (2003) used a bandwidth of 10 MHz, which is amongst the widest, to search for HI absorption towards 57 radio sources. They detected absorption towards 19 of these and found a variety of line profiles from Gaussians with a FWHM of $\lesssim 10 \text{ km s}^{-1}$ to irregular and multi-peaked profiles which sometimes span a few hundred km s^{-1} . However, the typical value is $\sim 150 \text{ km s}^{-1}$. Further, the velocities of the principal (strongest) absorption component with respect to the systemic velocity ranges from -1420 to $+318 \text{ km s}^{-1}$, with 16 of 19 ($\sim 85\%$) lying within the velocity range of $\pm 500 \text{ km s}^{-1}$. In this phase of our study of HI absorption towards radio sources, the velocity coverage for the Arecibo and GMRT observations were typically ~ 2500 and 1000 km s^{-1} respectively. The GMRT observations would hence not detect the highest-velocity components of Vermeulen et al., should these be present.

In the samples considered here, the spatial resolution was usually insufficient to resolve compact sources, while larger sources are often resolved. In order to have an average value of the HI optical depth, or an upper limit over the scale length of the radio source, we have considered only sources for which most of the radio continuum emission lies well within the resolution element of the telescopes. In some sources, HI absorption may be detected against a single component, such as the radio cores in PKS1318–43 and 3C353 (e.g. Morganti et al. 2001). We will consider such cases in a later paper, along with our HI absorption observations towards the cores and hotspots of radio sources.

With the above selection criterion, we obtain a sample of 96 radio sources, called the ‘full sample’, which is a heterogeneous superset of sources with available HI information. This sample is the combination of Tables 1 and 11, with the omission of J1643+1715 for which no HI data exists. Data for J0901+2901 was taken from Vermeulen et al. (2003), rather than from our own shallower observations of the source. The sample includes 27 GPS, 35 CSS, 13 CFS and 21 LRG sources (see Table 12). Amongst the GPS and CSS objects, 17 are associated with quasars, and 44 with

galaxies. All the CFS sources are associated with quasars or BL Lac objects, while the LRGs are associated with galaxies. The sample spans a wide range of ~ 6 orders of magnitude in luminosity at 5 GHz and $z \lesssim 1.4$. However, since most sources have been selected from strong flux-density limited samples, luminosity and redshift are strongly correlated (see Fig. 15).

4.2 HI column density versus linear size

For the ‘full sample’, Fig. 16 shows the 21-cm HI column density against projected linear size measured from the outermost peaks of radio emission. $T_s = 100 \text{ K}$ and full coverage of the background source have been assumed to estimate the column density using eqn. 1. The upper limits on $N(\text{HI})$ for non-detections are calculated from the 3σ limit on the peak optical depth as estimated from the spectrum or given in the literature, and a velocity width of 100 km s^{-1} . Fig. 16 shows that the incidence of HI absorption is much higher for the compact sources. In particular, for sources with sizes less than 15 kpc, HI absorption is detected towards 26 out of 75 ($\sim 35\%$), while only 5 out of 21 ($\sim 25\%$) LRG sources exhibit HI absorption. The detection rate ($\sim 45\%$) is maximum for the most compact class, the GPS sources (see Table 12).

The ‘full sample’ shows an anticorrelation between $N(\text{HI})$ and source size (Fig. 16), which was first noted by Pihlström et al. (2003) for the GPS and CSS sources. However, when interpreting this relationship, we need to bear in mind the uncertainties in the values of spin temperature and covering factor for the different objects. The small sources are capable of probing gas closer to the AGN so that T_s could be greater than 100 K. If this were so, it would only increase our estimate of the column density for the smaller sources thereby increasing the difference in HI column density between the smaller and the larger objects. The other factor influencing this relationship is the covering factor which could in principle increase the estimates of column density for the larger objects. This depends on the size of the absorber relative to the radio source and can be probed by high-resolution spectroscopic observations.

It is relevant to note that the above anti-correlation is consistent with the optical spectroscopic observations of van Ojik et al. (1997), who interpreted deep troughs in the $\text{Ly}\alpha$ emission profiles of 18 high-redshift ($z > 2$) radio galaxies (HZRGs) to be absorption due to HI with column densities in the range $10^{18} - 10^{19.5} \text{ cm}^{-2}$. Interestingly, 9 out of the 10 HZRGs with sizes $< 50 \text{ kpc}$ have associated HI absorption compared with 2 of the 8 larger ($> 50 \text{ kpc}$) ones.

4.3 HI column density versus redshift

The HST studies of distant galaxies ($z \lesssim 1$; e.g. Abraham et al. 1996; Brinchmann et al. 1998) show remarkable morphological evolution and suggest larger incidences of mergers and interactions in the past. Such mergers and interactions could trigger gas inflows towards the central regions of galaxies leading to the formation of circumnuclear starbursts, tori and the fuelling of nuclear black holes (Sanders et al. 1988; Hopkins et al. 2005). It is thus pertinent to enquire whether the environments of radio sources as probed by HI absorption bear any signature of evolution with redshift. In Fig. 17, we plot $N(\text{HI})$ against redshift for the ‘full sample’. Clearly,

Table 11. Sample of radio sources from literature forming the ‘full sample’.

Source name	Alt. name	Opt. ID	Redshift	$P_{5\text{GHz}}$ 10^{25} W/Hz	LAS "	LLS kpc	Ref.	Radio class	$N(\text{HI})$ 10^{20} cm $^{-2}$	V_{shift} km s $^{-1}$	Ref.
(1)	(2)	(3)	(4)	(5)	(6)	(7)	(8)	(9)	(10)	(11)	(12)
J0025–2602	OB-238	G	0.322	112	0.65	3.02	1	CSS	2.42	–30	V
J0111+3906	OC314	G	0.669	99	0.005	0.036	2,3	GPS	79.8	0	C1
						4.5					
J0141+1353	3C49	G	0.621	134	0.99	6.71	6,7	CSS	1.17	–185	V
J0157–1043	OC-192	Q	0.616	121	5.0	33.8	8	LRG	<1.00		V
J0201–1132	3C57	Q	0.669	219	1.7	11.9	8	CSS	<0.68		V
J0224+2750	3C67	G	0.310	25.8	2.5	11.3	7,9	CSS	<1.45		V
J0348+3353	3C93.1	G	0.243	13.6	0.56	2.14	10	CSS	<1.38		V
J0401+0036	3C99	G	0.426	33.8	4.2	23.3	11	LRG	<1.13		V
J0410+7656	4C76.03	G	0.599	336	0.14	0.93	7,10	CSS	2.66	315	V
J0431+2037	OF247	G	0.219	32.8	0.29	1.02	10,12	GPS	3.66	318	V
J0503+0203	OG003	Q	0.585	196	0.011	0.073	13	GPS	6.65	43	C1
J0521+1638	3C138	Q	0.759	78.6	0.68	4.98	6,7,14	CSS	<0.48		V
J0522–3627	MRC	G	0.0553	5.6	8.3	9.1	15	CSS	<0.39		M
J0542+4951	3C147	Q	0.545	841	0.94	5.98	16	CSS	<0.30		V
J0556–0241		G	0.235	4.6	0.02	0.09	17	GPS	<6.27		V
J0609+4804	3C153	G	0.277	34.7	5.4	22.4	11	LRG	<0.65		V
J0627–3529	MRC	G	0.0546	1.5	0.21	0.23	18	CFS	<1.35		M
J0741+3112	OI363	Q	0.635	237	0.006	0.042	13,19	GPS	<0.99		V
J0815–0308	3C196.1	G	0.198	3.0	3.0	9.7	11	CSS	<1.53		V
J0834+5534	4C55.16	G	0.242	85	11.0	41.4	20	LRG	1.14	–399	V
J0901+2901	3C213.1	G	0.194	7.4	5.7	18.2	21	LRG	0.12	–14	V
J0909+4253	3C216	Q	0.670	301	9.2	64.5	22	LRG	1.30	102	V
J0927+3902	4C39.25	Q	0.695	654	3.1	22.1	23	LRG	<0.99		V
J0939+8315	3C220.3	G	0.685	145	7.8	55.1	24	LRG	<0.49		V
J0943–0819		G	0.228	15.5	0.020	0.072	25	GPS	<1.27		V
J0954+7435		G	0.695	462	0.021	0.150	26,27	GPS	<2.51		V
J1035+5628	OL553	G	0.459	72.0	0.034	0.020	28	GPS	<1.38		V
J1104+3812	Mrk421	G	0.0300	0.14	0.075	0.044	29	CFS	<1.16		G
J1120+1420	4C14.41	G	0.362	37.7	0.084	0.420	30	GPS	<0.61		V
J1159+2914	4C29.45	Q	0.729	241	5.4	39.1	31	LRG	<1.91		V
J1206+6413	3C268.3	G	0.371	55.0	1.3	6.6	7,16	CSS	2.07	258	V
J1220+2916	NGC4278	G	0.0022	0.0003	0.029	0.001	32	CFS	<2.12		G
J1252+5634	3C277.1	Q	0.321	26.8	1.7	7.7	7,16	CSS	<0.72		V
J1308–0950	OP-010	G	0.464	166	0.60	3.47	1	CSS	<1.35		V
J1313+5458		Q	0.613	72.0	0.037	0.250	26	GPS	<1.80		V
J1326+3154	4C32.44	G	0.370	88.7	0.056	0.285	33,34	GPS	0.75	–471	V
J1356+0515	NGC5363	G	0.004	0.0004	<1.0	<0.08	35	CFS	10.3	96	G
J1357+4354		G	0.646	58.6	0.017	0.117	36	GPS	35.42	–165	V
J1400+6210	4C62.22	G	0.431	108	0.065	0.362	10	GPS	1.99	–258	V
J1407–2701	IC4374	G	0.022	0.056	0.009	0.004	25	CFS	<3.28		G
J1415+1320	OQ122	G/Q	0.247	12.9	0.114	0.437	27,37	CSS	10.60	0	C2
J1421+4144	3C299	G	0.367	39.4	11.2	56.7	21	LRG	<0.70		V
J1443+7707	3C303.1	G	0.267	10.1	1.8	7.3	16	CSS	<1.50		V
J1540+1447	4C14.60	Q	0.605	120	4.0	26.8	38	LRG	<0.62		V
J1546+0026		G	0.550	104	0.010	0.064	27	GPS	<1.05		V
J1556–7914	MRC	G	0.1501	24.8	0.120	0.300	39	CFS	3.82		M
J1642+6856	4C69.21	Q	0.751	236	8.3	61.0	40	LRG	<1.34		V
J1653+3945	Mrk501	G	0.034	0.35	0.025	0.017	29	CFS	<4.44		G
J1658+0741	OS092	Q	0.621	130	7.1	48.2	40	LRG	<1.56		V
J1815+6127		Q	0.601	54.2	0.010	0.068	26	GPS	4.61	–1258	V
J1816+3457		G	0.245	5.6	0.039	0.149	27	CSS	5.40	–184	P1
J1819–6345	MRC	G	0.0645	4.2	0.33	0.400	1,42	CSS	21.2	–160	M
J1821+3942	4C39.56	G	0.798	319	0.47	3.53	10,12	CSS	1.75	–806	V
J1823+7938		G	0.224	6.3	0.015	0.054	26	GPS	<26.7		V
J1829+4844	3C380	Q	0.692	912	1.3	9.0	16	CSS	<0.19		V
J1831+2907	4C29.56	G	0.842	357	2.6	19.9	43	LRG	<1.70		V
J1845+3541	OU373	G	0.764	126	0.010	0.071	44	GPS	<11.0		V
J1944+5448	OV573	G	0.263	17.3	0.040	0.161	12,44	GPS	5.21	–1420	V
J1945+7055		G	0.101	1.5	0.035	0.064	45	GPS	30.0	–172	P2

Table 11 – continued

Source name	Alt. name	Opt. ID	Redshift	$P_{5\text{GHz}} \times 10^{25}$ W/Hz	LAS "	LLS kpc	Ref.	Radio class	$N(\text{H}\alpha) \times 10^{20}$ cm $^{-2}$	V_{shift} km s $^{-1}$	Ref.
(1)	(2)	(3)	(4)	(5)	(6)	(7)	(8)	(9)	(10)	(11)	(12)
J2022+6136	OW637	Q	0.227	32.4	0.010	0.036	28	GPS	<0.38		V
J2052+3635		G	0.355	117	0.060	0.297	46	GPS	7.69	-95	V
J2137-2042	OX-258	G	0.635	223	0.200	1.370	1,47	CSS	<1.18		V
J2151+0552		G	0.74	112	0.004	0.027	48	GPS	<16.9		C1
J2202+4216	DA571	Q	0.069	3.8	0.010	0.013	2	CFS	<1.74		G
J2209-2331	MRC	G	0.087	1.7	<2.0	<3.2	49	CSS	<1.35		G
J2255+1313	3C455	Q	0.543	102	2.6	16.5	21	LRG	0.45	30	V
J2257-3627	MRC	G	0.006	0.009	0.030	0.004	47	CFS	<1.74		G
J2321+2346	3C460	G	0.268	9.4	5.8	23.7	41	LRG	<2.04		V
J2333-2343	OZ-252	G	0.048	0.46	0.037	0.034	28	CFS	<1.54		G
J2344+8226		Q	0.735	292	0.267	1.940	10,12	GPS	<0.75		V
J2355+4950	OZ488	G	0.238	22.3	0.069	0.256	50,51	GPS	3.01	-12	V

Col. 1: source name; col. 2: alternative name; col. 3: optical identification; col. 4: redshift; col. 5: 5-GHz luminosity in the rest frame of the source; cols. 6 & 7: largest projected angular (LAS) and linear (LLS) size in arcsec and kpc respectively, as measured from the outermost radio peaks; col. 8: references for the radio structure; col. 9: radio class; col. 10: H α column density or a 3σ upper limit to it; col. 11: the shift of the primary H α component relative to the systemic velocity as measured from the optical emission lines, with a negative sign indicating a blue-shift, and column 12: references for the H α observations.

References for the structural information and LLS: 1: Tzioumis et al. (2002); 2: Pearson & Readhead (1988); 3: Owsianik, Conway & Polatidis (1998); 4: Zensus et al. (2002); 5: Baum et al. (1990); 6: Fanti et al. (1989); 7: Saikia et al. (1995); 8: Reid, Kronberg & Perley (1999); 9: Sanghera et al. (1995); 10: Dallacasa et al. (1995); 11: Neff, Roberts & Hutchings (1995); 12: Saikia et al. (2001); 13: Stanghellini et al. (2001); 14: Akujor et al. (1991); 15: Keel (1986); 16: Lüdke et al. (1998); 17: Petrov et al. (2005); 18: Venturi et al. (2000); 19: Saikia & Kulkarni (1998); 20: Whyborn et al. (1985); 21: Akujor & Garrington (1995); 22: van Breugel et al. (1992); 23: Browne et al. (1982); 24: Jenkins, Pooley & Riley (1977); 25: Beasley et al. (2002); 26: Taylor et al. (1994); 27: Peck et al. (2000); 28: Fomalont et al. (2000); 29: Giovannini, Feretti & Venturi (1999); 30: Bondi, Garrett & Gurvits (1998); 31: Antonucci & Ulvestad (1985); 32: Giovannini et al. (2001); 33: Mutel et al. (1981); 34: Fey, Clegg & Fomalont (1996); 35: van Gorkom et al. (1989); 36: Taylor et al. (1996); 37: Perlman et al. (1996); 38: Ulvestad, Johnston & Weiler (1983); 39: Morganti et al. (2001); 40: Murphy, Browne & Perley (1993); 41: Giovannini et al. (1988); 42: Ojha et al. (2004); 43: Spencer et al. (1989); 44: Xu et al. (1995); 45: Taylor & Vermeulen (1997); 46: Philips & Mutel (1981); 47: Fomalont et al. (2003); 48: Stanghellini, O'Dea & Murphy (1999); 49: Kapahi et al. (1998a); 50: Polatidis et al. (1995); 51: Taylor et al. (2000).

References for H α observations: C1: Carilli et al. (1998); C2: Carilli et al. (1992); M: Morganti et al. (2001); G: van Gorkom et al. (1989); M: Morganti et al. (2001); P1: Peck et al. (2000); P2: Peck, Taylor & Conway (1999); V: Vermeulen et al. (2003)

a Errors in the systemic velocity are too large.

no trend exists for N(H α) to vary with redshift out to $z \sim 1$. However, it is possible that any such dependence is not apparent for the ‘full sample’ as it contains sources with luminosities and projected linear sizes spanning a range of ~ 6 orders of magnitude in luminosity and 4–5 orders of magnitude in linear size. The parameter space can be constrained to some extent by considering the sub-sample consisting of just GPS and CSS sources. This sub-sample contains 62 sources with projected linear size ≤ 15 kpc, $\sim 85\%$ of which have luminosities spanning ~ 2 orders of magnitude. In Fig. 18, we plot the redshift distributions of these GPS and CSS sources separately for H α detections and non-detections. There is again no significant difference between the two redshift distributions, suggesting that the environments of radio sources on GPS and CSS scales as probed by the neutral gas component are similar at different redshifts. Interestingly, this is consistent with the polarization asymmetry study of CSS and larger sources by Saikia & Gupta (2003), whose sample of sources with $z \lesssim 2$, showed no significant dependence of polarization asymmetry on redshift. A study of the fraction of CSS objects at different redshifts in well-defined complete samples led Röttgering et al. (1996)

Table 12. Summary of the ‘full sample’.

Radio class.	Detections	Non-detections
GPS	12	15
CSS	11	24
CFS	3	10
LRG	5	16

to suggest that the environments of CSS objects do not vary significantly with redshift.

4.4 H α column density versus luminosity

It is widely believed that the energy output from AGN is triggered by the supply of gas to the central engine, presumably a supermassive black hole (e.g. Rees 1984). Although there have been a number of studies of gas kinematics of nearby AGN in order to understand the fuelling of such activity, the dependence of N(H α) on radio luminosity could provide clues towards understanding this phenomenon. In Fig. 19, we plot N(H α) against the radio luminosity at 5

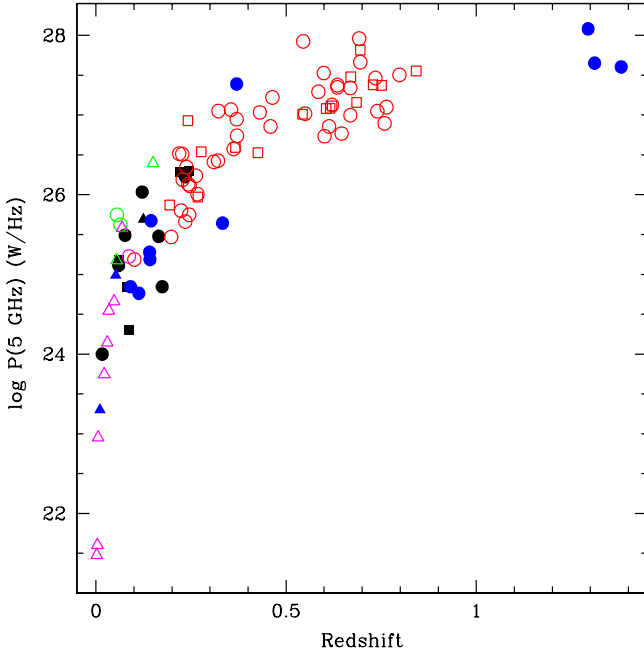


Figure 15. Luminosity of sample sources at 5 GHz versus redshift. The solid symbols are sources from our observations, while open symbols are data from the literature. The circles denote GPS/CSS, triangles CFS, and squares LRG sources. For our observations, black represents Arecibo sources and blue the GMRT’s. Red corresponds to data from Vermeulen et al. (2003) and Pihlström et al. (2003), green to Morganti et al. (2001) and magenta to van Gorkom et al. (1989).

GHz for the ‘full sample’. There is no significant dependence of $N(\text{HI})$ on radio luminosity. Since luminosity and redshift are strongly correlated in our sample, and there is no significant dependence of $N(\text{HI})$ on redshift, this is not surprising. In order to investigate any dependence of $N(\text{HI})$ on luminosity, one requires objects with HI detections covering a large range in luminosity but confined to a narrow range in redshift for a given class of objects. Although the ‘full sample’ contains objects spanning ~ 4 orders of magnitude in luminosity in the lowest redshift range, these are a “mixed bag” with very few HI detections. To address this issue satisfactorily, one needs to extend the HI observations of radio sources, especially GPS and CSS sources, to lower luminosities of (say) 10^{24} to 10^{26} W Hz $^{-1}$ at 5 GHz in the redshift range of ~ 0.5 to 1.

4.5 HI absorption and unification scheme

GPS and CSS sources are believed to be young, seen at an early stage of their evolution. Though it is possible that a few (e.g. 3C216) have small linear sizes due to projection effects, most are intrinsically compact (Fanti et al. 1990). An interesting question is whether GPS and CSS objects are consistent with the unification scheme for radio galaxies and quasars, in which quasars are inclined at $\lesssim 45^\circ$ to the line of sight while galaxies lie at larger angles (Barthel 1989; Antonucci 1993). Saikia et al. (1995, 2001) have argued from the prominence of their radio cores and their symmetry pa-

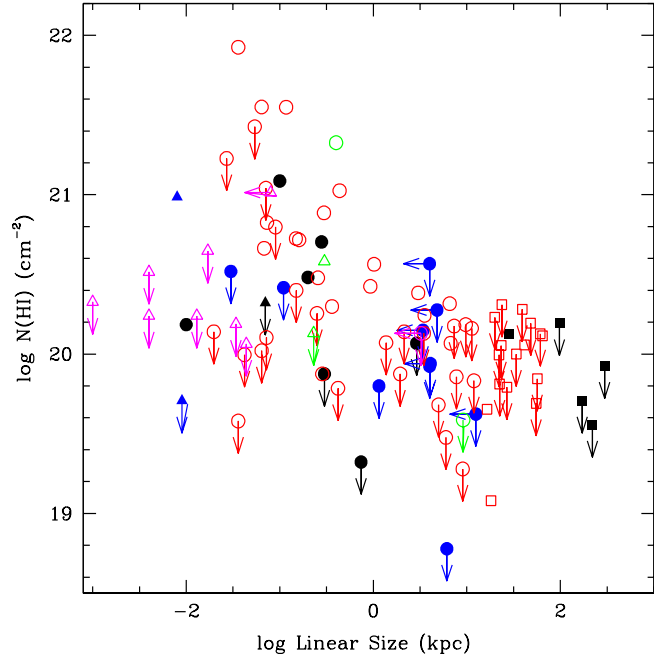


Figure 16. HI column density as a function of projected linear source size. Arrows mark the 3σ upper limit to the column density or to the linear size. See the caption of Fig. 15 for the meaning of the colours and symbols.

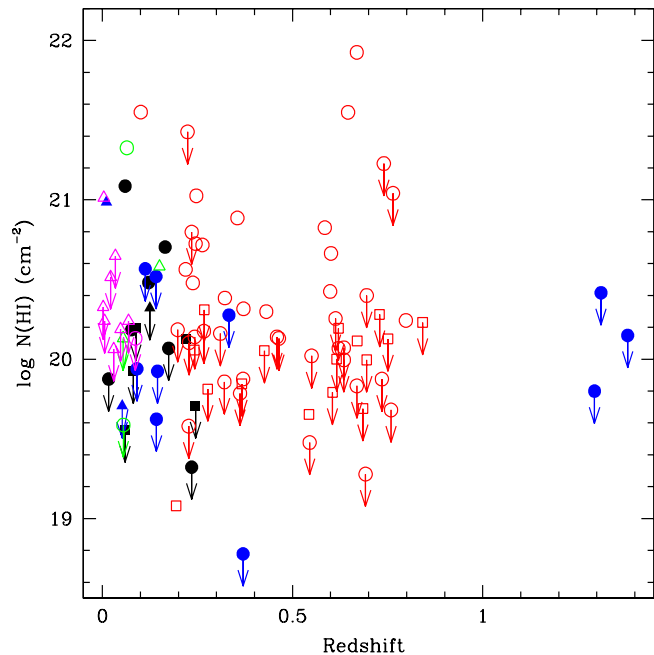


Figure 17. HI column density versus redshift. See the caption of Fig. 15 for the meaning of the colours and symbols.

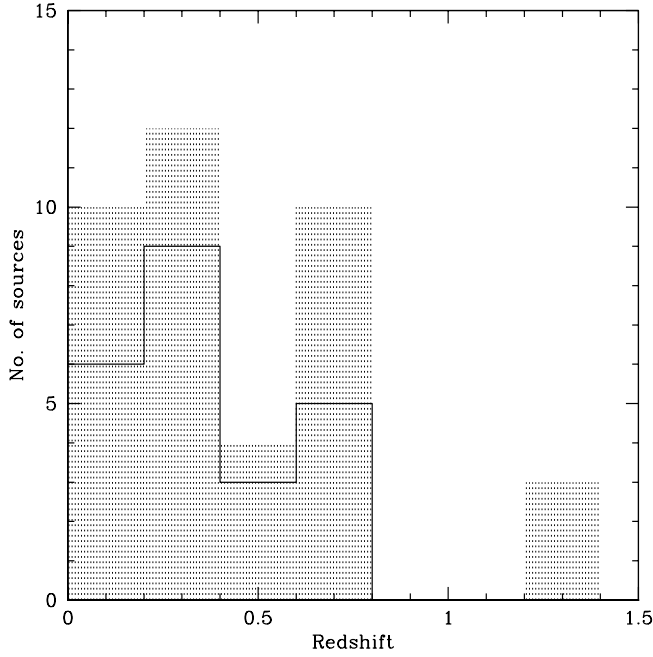


Figure 18. The redshift distribution of GPS and CSS sources with detections (solid lines) and non-detections (shaded).

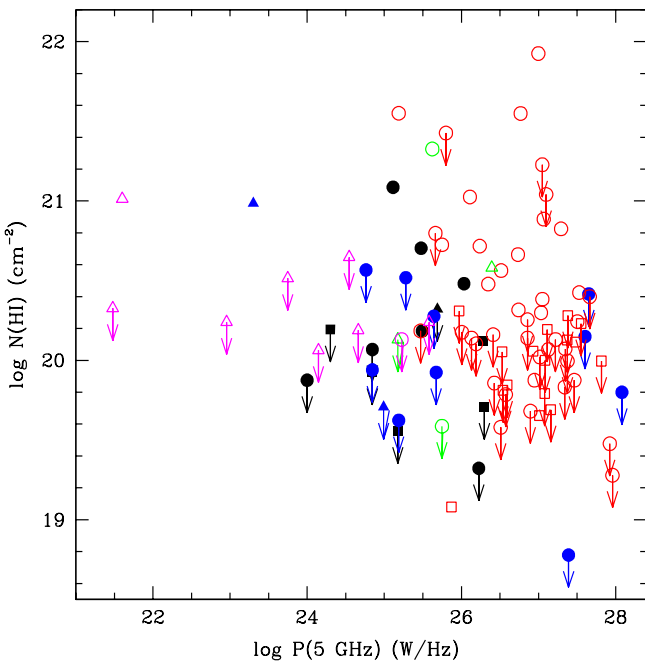


Figure 19. HI column density versus source luminosity at 5 GHz. See the caption of Fig. 15 for the meaning of the colours and symbols.

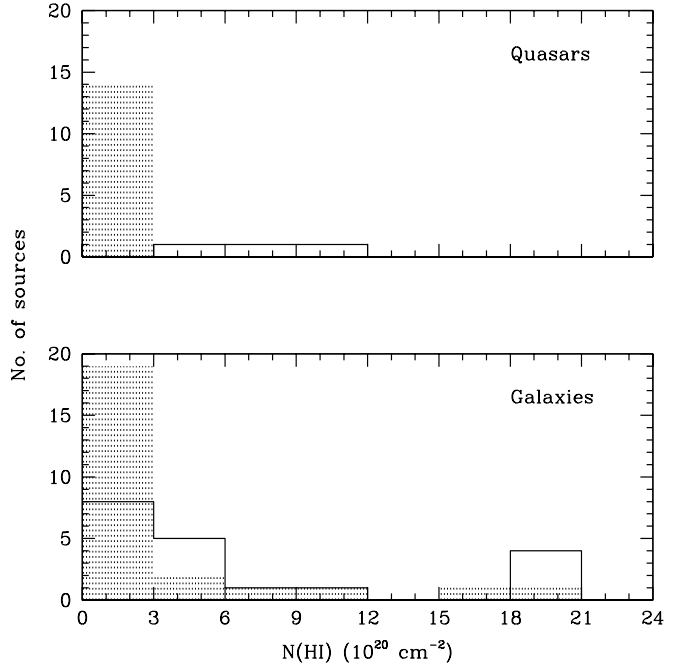


Figure 20. The HI column density distribution of GPS and CSS quasars (top panel) and galaxies (bottom panel). The detections are marked by solid lines while the shaded regions represent non-detections. The four detections and one non-detection for galaxies with $\log N(\text{HI}) > 19.5$ have been put in the last bin.

rameters that GPS and CSS objects are also consistent with the unified scheme. If this is so, then one might also expect a dependence of the detection rate of HI absorption and HI column density on the optical identification of the parent optical object and the fraction of emission from the core (Pihlström et al. 2003), which is a reasonable statistical indicator of the source-axis orientation to the line of sight (Orr & Browne 1982; Kapahi & Saikia 1982). The exact nature of the variation would depend on the form of the disk or torus, which is not well constrained.

As a first step, we examine whether the detection rate for the ‘full sample’ is consistent with the unification scheme. In Fig. 20, we plot the $N(\text{HI})$ distributions for GPS and CSS quasars and galaxies. Clearly, the detection rate ($\sim 40\%$) for galaxies is higher than that ($\sim 20\%$) for quasars. Considering just the GPS and CSS objects separately, one finds for both a similar difference in the detection rates for galaxies and quasars. This is consistent with the unification scheme for radio galaxies and quasars (e.g. Pihlström et al. 2003). In addition to the geometries considered by Pihlström et al., the distribution of HI gas clouds is likely to be anisotropic since those close to the path of the radio jet, or within the ionisation cone, are more likely to be ionised than those at larger angles to the jet axis (cf. van Ojik et al. 1997). This could also cause a higher detection rate of HI absorption in galaxies relative to quasars in the framework of orientation-based unification schemes.

Gupta & Saikia (2006) have recently reported the consistency of HI properties with the unification scheme for radio galaxies and quasars selected from this ‘full sample’. They have shown that there is a tendency for the detection

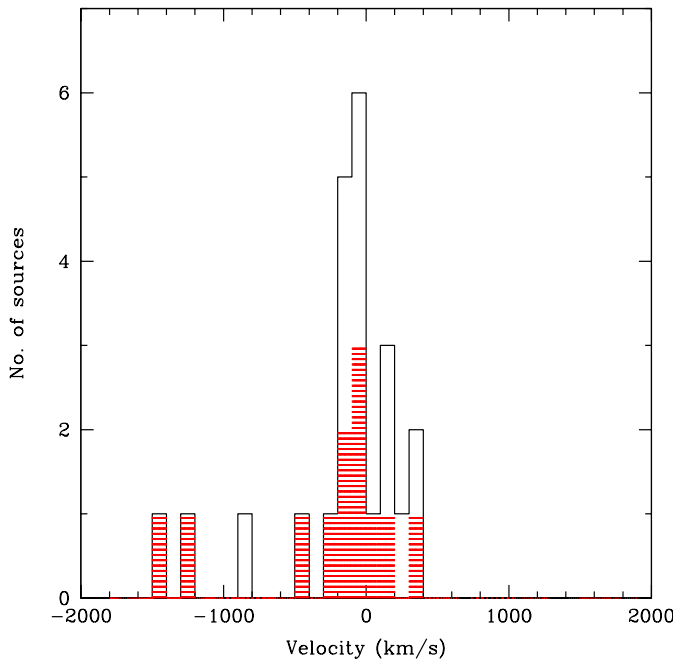


Figure 21. The distribution of velocities for the principal HI absorption components with respect to the systemic velocity estimated from optical lines. The solid line is the distribution for both CSS and GPS sources, while the distribution for GPS sources is shown shaded.

rate as well as the column density for galaxies to increase with core prominence, a statistical indicator of the orientation of the jet axis to the line of sight. This can be understood in a scenario where radio sources are larger than the scale of the circumnuclear HI disc so that the lines of sight to the lobes at very large inclinations do not intersect the disc. They also suggest that small linear size, along with intermediate values of core prominence, is a good recipe for detecting 21-cm absorption in CSS and GPS objects.

4.6 Blue-shifted absorption lines: Evidence of jet-cloud interaction?

Although blue-shifted absorption lines could arise due to either halo gas or circumnuclear gas kinematically affected by nuclear winds and/or radiation pressure, the jet-cloud interaction may also play a significant role in sub-galactic sized radio sources. The structure of GPS and CSS sources often appear to be affected by the ambient gas, suggesting dynamical interaction with the external medium (Spencer et al. 1991; Schilizzi et al. 2000). In particular, CSS sources tend to be more asymmetric in brightness, location and polarization of the outer radio components when compared with the larger sources (Saikia et al. 1995, 2001; Arshakian & Longair 2000; Saikia & Gupta 2003). They also tend to exhibit high rotation measures (see O'Dea 1998 for a review). The properties of emission-line gas in the galaxies associated with these sources are also consistent with the scenario in which ambient gas has been ionized and accelerated by shocks caused by interaction with the radio jet (Gelderman & Whittle 1994; Labiano et al. 2005). In the archetypal

CSS object 3C48, the kinematical properties of the blue-shifted gas seen in emission and absorption (Chatzichristou et al. 1999; Gupta et al. 2005) suggest that the complex radio structure of the source (Wilkinson et al. 1991) could be caused by interaction of the jet with the external gas clouds. Baker et al. (2002) studied absorption spectra for a sample of quasars from the Molonglo Reference Catalogue, and find a slight excess of blue-shifted C IV absorption lines in CSS sources as compared with the larger objects. van Ojik et al. (1997) also found an excess of blue-shifted Ly α absorption lines in their sample of HZRGs, and demonstrated strong evidence for interaction of the radio sources with the external environment. In principle jet-cloud interaction can give rise to blue-shifted as well as red-shifted absorption lines. However, 21-cm absorption line experiments towards a sample of sources which are randomly oriented towards us could exhibit an excess of blue-shifted lines. This is because for the sources oriented significantly away from the sky plane, a) the approaching jet will be stronger than the receding jet due to Doppler boosting and b) the absorbing gas towards the approaching hot-spot/lobe is likely to have a larger covering factor. These effects possibly play a role in the fact that broad (~ 1000 km s $^{-1}$) 21-cm absorption lines towards radio sources, which are believed to have been caused by jet-cloud interaction, are all blue-shifted (Morganti, Tadhunter & Oosterloo 2005).

In Fig. 21, we plot the distribution of the velocity shifts of the principal (strongest) 21-cm absorption component detected towards the CSS and GPS sources in the 'full sample'. Though hampered by small number statistics, and uncertainties in systemic velocities (cf. Mirabel 1989; Morganti et al. 2001), the distribution does indicate that HI absorption for compact radio sources tends to be blue-shifted, with 14 out of the 23 principal absorption-line components displaying such an effect. We note that the skewness of the distribution comes largely from the principal components detected towards GPS sources. Of the 12 principal components detected towards GPS sources 8 have blue-shifted velocities with respect to the systemic velocity. Also, 6 of the 9 secondary components listed by Vermeulen et al. (2003) appear blue shifted. The higher incidence of blue-shifted features suggests that some of the absorption could be due to gas clouds accelerated by the radio jets.

4.7 OH upper limits and their implications

The parameters of the 9 OH non-detections at Arecibo are given in Table 13. Upper limits on thermal OH column densities can be calculated using

$$N(OH) = 2.25 \times 10^{14} \frac{T_{\text{ex}} \int \tau_{1667}(v) dv}{f_c} \text{ cm}^{-2} \quad (2)$$

where $\tau_{1667}(v)$ is the optical depth in the 1667.3-MHz OH main-line at radial velocity v km s $^{-1}$ (e.g. Boyce & Cohen 1994). Below, a covering factor of $f_c=1.0$ and an excitation temperature of $T_{\text{ex}} = 10$ K are adopted.

Assuming that a velocity equivalent width from the HI absorption of $v_{eq} = \int \tau_{HI}(v) dv / \tau_p$ also applies to any OH absorption, we have computed upper limits on the OH column densities for the three sources for which both an HI absorption was detected at Arecibo and an upper limit obtained on OH absorption. An optical depth limit for OH ab-

sorption of $3 \times \sigma_{\text{FA}}^{\text{OH}}$ was adopted, where $\sigma_{\text{FA}}^{\text{OH}}$ is taken from Table 2. This gives column densities of $< 1.1 \times 10^{14} \text{ cm}^{-2}$ for J1124+1919, $< 3.3 \times 10^{14} \text{ cm}^{-2}$ for J1347+1217, and $< 10.9 \times 10^{14} \text{ cm}^{-2}$ for J2316+0405. Of course, these upper limits need to be interpreted in the light of the expected covering factors for potential absorbers obtained from VLBI imaging and the projected angular sizes for diffuse clouds and giant molecular clouds (GMCs). However, we note that in our Galaxy, the column densities of OH in respect of diffuse clouds are of the order of $N(\text{OH}) \sim 10^{13-14} \text{ cm}^{-2}$, while typical values for GMCs are $N(\text{OH}) \sim 10^{15-16} \text{ cm}^{-2}$. The above column densities for HI and OH imply an abundance ratio of $N(\text{HI})/N(\text{OH}) \geq 4.4 \times 10^6$ for J1124+1919, the source with the lowest limit on $N(\text{OH})$, given the values adopted for HI and OH temperatures, and assuming similar covering factors. Other upper limits for $N(\text{OH})$ in Table 13 are 3σ values, assuming a velocity width of 100 km s^{-1} . It is worth noting for comparison that although there are only a few OH main-line absorption systems seen towards extragalactic sources, the typical column density for the detected ones is a few times $\sim 10^{15} \text{ cm}^{-2}$ (e.g. Darling & Giovanelli 2002; Kanekar & Chengalur 2002).

The non-detection of megamaser emission in the 1667-MHz OH main line provides us with upper limits on (isotropic) luminosities for this line. Adopting exactly the prescription used for their non-detections by Darling & Giovanelli (2002), which assumes a line intensity of 1.5σ , a rest-frame velocity width of 150 km s^{-1} , and normalization to $H_0 = 75 \text{ km s}^{-1} \text{ Mpc}^{-1}$, $q = 0$, upper limits have been computed for the 9 sources for which good OH spectra were obtained. These luminosity limits, $L_{\text{OH}}^{\text{max}}$, are given in Table 13 and agree within 5% with the estimated luminosities were the same cosmological parameters to be adopted as in the rest of this paper. Of these, only J1347+1217 and J2316+0405 were detected by IRAS. From the $L_{\text{OH}} - L_{\text{FIR}}$ relationship of Kandalian (1996), Darling & Giovanelli predict luminosity values for these of $L_{\text{OH}} = 2.36$ and $2.46 h_{75}^{-2} L_{\odot}$ respectively. While our luminosity upper limit for J2316+0405 is about a factor of 4 higher than the predicted OH luminosity, that for J1347+1217 is somewhat below the predicted value. As mentioned in Section 3.3, obtaining a spectrum of increased sensitivity for J1347+1217 would be valuable.

In respect of the non-detection of OH emission for any of the AGNs observed by us, we note that Darling & Giovanelli (2000) failed to detect any OH megamasers for a sample of nearby AGNs situated in quiescent (non-interacting) systems and which were undetected by IRAS.

5 SUMMARY

We have presented results from a search for associated HI absorptions towards 27 radio sources using the Arecibo and GMRT telescopes. We detect HI absorption towards six and HI emission from one. A totally new HI absorption system was detected against the radio galaxy 3C258, whose HST image shows an odd-shaped galaxy with an arc-like structure of high surface brightness, and a larger, fainter tail extending to the northeast. The HI absorption spectrum is complex, possibly due to interaction of the compact radio source with the ISM of the host galaxy.

Table 13. Results of the Arecibo search for associated OH absorption.

Source name	Date	$\sigma_{\text{FA}}^{\text{OH}} 10^{-3}$	Δv^{OH} km s $^{-1}$	$N(\text{OH}) 10^{14} \text{ cm}^{-2}$	$\log L_{75}^{\text{max}} h_{75}^{-2} L_{\odot}$
J0034+3025	2002 Dec	2.0	13.6	< 13.5	< 1.99
J0645+2121	2002 Dec	0.79	15.3	< 5.3	< 2.89
	2004 Sep				
J0725-0054	2002 Dec	2.1	12.6	< 14.2	< 2.48
	2002 Dec				
J0901+2901	2002 Nov	0.46	14.1	< 3.1	< 2.34
	2002 Dec				
J1124+1919	2002 Nov	0.61	13.4	< 1.1	< 1.96
	2003 Jan				
J1347+1217	2002 Nov	0.37	12.4	< 3.3	< 2.25
	2003 Jan				
J1643+1715	2004 Mar	0.44	13.3	< 3.0	< 2.42
J2250+1419	2002 Dec	0.38	15.1	< 2.6	< 2.41
J2316+0405	2002 Dec	0.76	14.7	< 10.9	< 3.03

Col. 1: source name; col. 2: dates of the observations; col. 3 & 4: 1σ noise for the OH fractional absorption, and the corresponding velocity resolution; cols. 5 & 6: upper limits on OH column density and luminosity, respectively.

We have also presented the results of OH observations towards 9 sources using the Arecibo telescope. No OH was detected towards any of these sources either in emission or absorption. The estimated column densities for HI and OH imply an abundance ratio of $N(\text{HI})/N(\text{OH}) \gtrsim 4 \times 10^6$ for 3C258, adopting typical values for HI and OH temperatures and assuming similar covering factors.

We combine our HI results with similar, previously published, searches to obtain a ‘full sample’ of 96 radio sources consisting of 27 GPS, 35 CSS, 13 CFS and 21 LRG radio sources. The resultant sample has sources with 5-GHz integrated powers spread over ~ 6 orders of magnitude and with redshifts up to $z \sim 1.4$. In the ‘full sample’ we find that the HI absorption detection rate is highest ($\sim 45\%$) for the compact GPS sources and least ($\sim 25\%$) for the large LRG sources. The anticorrelation between the HI column density and source size for GPS and CSS sources, first noted by Pihlström et al. (2003), is confirmed by this enlarged sample. This anticorrelation is also consistent with the optical spectroscopic results of van Ojik et al. (1997) as described in Section 4.2.

The HI column density, as probed by 21-cm absorption, shows no significant dependence on redshift for the ‘full sample’ or for the sub-sample of GPS and CSS sources, suggesting that the environments on these scales are similar for different redshifts. This is consistent with finding no significant dependence of polarization asymmetry of the lobes of these sources on redshift (Saikia & Gupta 2003), and also the fraction of these small sources being similar at different redshifts (Röttgering et al. 1996).

For the subsample of CSS and GPS sources, the HI detection rate is higher ($\sim 40\%$) for galaxies than for quasars ($\sim 20\%$). This is consistent with the unification scheme. The principal (strongest) absorption component detected towards GPS sources appears to be blue-shifted in 65% of the cases. This could be due to the interaction of radio sources with the ambient environment.

ACKNOWLEDGMENTS

We thank Rene Vermeulen, the referee, and Ralph Spencer for many useful suggestions and comments. We thank the staffs of the Arecibo telescope and GMRT for their assistance during our observations. The Arecibo Observatory is part of the National Astronomy and Ionosphere Center, which is operated by Cornell University under a cooperative agreement with the National Science Foundation. The GMRT is a national facility operated by the National Centre for Radio Astrophysics of the Tata Institute of Fundamental Research. We thank numerous contributors to the GNU/Linux group. This research has made use of the NASA/IPAC Extragalactic Database (NED) which is operated by the Jet Propulsion Laboratory, California Institute of Technology, under contract with the National Aeronautics and Space Administration.

REFERENCES

Abraham R.G., van den Bergh S., Glazebrook K., Ellis R.S., Santiago B.X., Surma P., Griffiths R.E., 1996, ApJS, 107, 1

Akujor C.E., Garrington S.T., 1995, A&AS, 112, 235

Akujor C.E., Spencer R.E., Zhang F.J., Davis R.J., Browne I.W.A., Fanti C., 1991, MNRAS, 250, 215

Antonucci R., 1993, ARA&A, 31, 473

Antonucci R.R.J., Ulvestad J.S., 1985, ApJ, 294, 158

Arshakian T.G., Longair M.S., 2000, MNRAS, 311, 846

Baker J.C., Hunstead R.W., Athreya R.M., Barthel P.D., de Silva E., Lehnert M.D., Saunders R.D.E., 2002, ApJ, 568, 592

Barthel P.D., 1989, ApJ, 336, 606

Baum S.A., Heckman T., Bridle A., van Breugel W., Miley G., 1988, ApJS, 68, 643

Baum S.A., O'Dea C.P., de Bruyn A.G., Murphy D.W., 1990, A&A, 232, 19

Beasley A.J., Gordon D., Peck A.B., Petrov L., MacMillan D.S., Fomalont E.B., Ma C., 2002, ApJS, 141, 13

Bondi M., Padrielli L., Fanti R., Ficarra A., Gregorini L., Mantovani F., 1996, A&AS, 120, 89

Bondi M., Garrett M.A., Gurvits L.I., 1998, MNRAS, 297, 559

Boyce P.J., Cohen R.J., 1994, A&AS, 107, 563

Briggs F.H., Sorar E., Taramopoulos A., 1993, ApJ, 415, 99

Brinchmann J. et al., 1998, ApJ, 499, 112

Browne I.W.A., Orr M.J.L., Davis R.J., Foley A., Muxlow T.W.B., Thomasson P., 1982, MNRAS, 198, 673

Capetti A., de Ruiter H.R., Fanti R., Morganti R., Parma P., Ulrich M.H., 2000, A&A, 362, 871

Carilli C.L., Perlman E.S., Stocke J.T., 1992, ApJ, 400, L13

Carilli C.L., Menten K.M., Reid M.J., Rupen M.P., Yun M.S., 1998, ApJ, 494, 175

Chamaraux P., Balkowski C., Fontanelli I.P., 1987, A&AS, 69, 263

Chatzichristou E.T., Vanderriest C., Jaffe W., 1999, A&A, 343, 407

Conway J.E., 1999, NewAR, 43, 509

Conway J.E., Blanco P.R., 1995, ApJ, 449, 131

Cotton W.D., Feretti L., Giovannini G., Venturi T., Lara L., 1995, ApJ, 452, 605

Dallacasa D., Fanti C., Fanti R., Schilizzi R.T., Spencer R.E., 1995, A&A, 295, 27

Darling J., Giovanelli R., 2000, NAIC Newsletter No. 31, p. 7

Darling J., Giovanelli R., 2002, AJ, 124, 100

de Breuck C., Röttgering H., Miley G., van Breugel W., Best P., 2000, A&A, 362, 519

de Vaucouleurs G., de Vaucouleurs A., Corwin H.G. Jr., Buta R.J., Paturel G., Fouque P., 1991, Third Reference Catalogue of Bright Galaxies, Springer-Verlag, Berlin

de Vries W. H. et al., 1997, ApJS, 110, 191

Dey A., van Breugel W.J.M., 1994, AJ, 107, 1977

Dickey J.M., Planesas P., Mirabel I.F., Kažes I., 1990, AJ, 100, 1457

Eracleous M., Halpern J.P., 2004, ApJS, 150, 181

Fanti C. et al., 1989, A&A, 217, 44

Fanti R., Fanti C., Schilizzi R.T., Spencer R.E., Nan Rendong, Parma P., van Breugel W.J.M., Venturi T., 1990, A&A, 231, 333

Feng W.X., An T., Hong X.Y., Zhao Jun-Hui, Venturi T., Shen Z.-Q., Wang W.H., 2005, A&A, 434, 101

Fey A.L., Clegg A.W., Fomalont E.B., 1996, ApJS, 105, 299

Fey A.L., Charlot P., 1997, ApJS, 111, 95

Fey A.L., Charlot P., 2000, ApJS, 128, 17

Fomalont E.B., 1971, AJ, 76, 513

Fomalont E.B., Bridle A.H., 1978, AJ, 83, 725

Fomalont E.B., Frey S., Paragi Z., Gurvits L.I., Scott W.K., Taylor A.R., Edwards P.G., Hirabayashi H., 2000, ApJS, 131, 95

Fomalont E.B., Petrov L., MacMillan D.S., Gordon D., Ma C., 2003, AJ, 126, 2562

Gelderman R., Whittle M., 1994, ApJS, 91, 491

Ghosh T., Salter C.J., 2002, ASPC, 278, 521

Gilmore G., Shaw M.A., 1986, Nature, 321, 750

Giovannini G., Feretti L., Gregorini L., Parma P., 1988, A&A, 199, 73

Giovannini G., Feretti L., Venturi T., 1999, ASPC, 159, 439

Giovannini G., Cotton W.D., Feretti L., Lara L., Venturi T., 2001, ApJ, 552, 508

Gupta Neeraj, Srianand R., Saikia D.J., 2005, MNRAS, 361, 451

Gupta Neeraj, Saikia D.J., 2006, MNRAS, 370, 738

Heckman T.M., Balick B., van Breugel W.J.M., Miley G.K., 1983, AJ, 88, 583

Holt J., Tadhunter C.N., Morganti R., 2003, MNRAS, 342, 227

Hopkins P.F., Hernquist L., Cox T.J., Di Matteo T., Martini P., Robertson B., Springel V., 2005, ApJ, 630, 705

Huchra J.P., Geller J.M., de Lapparent V., Corwin Jr., H.G., 1990, ApJS, 72, 433

Jenkins C.J., Pooley G.G., Riley J.M., 1977, MmRAS, 84, 61

Kandalan R.A., 1996, Astrophysics, 39, 237

Kanekar N., Chengalur J.N., 2002, A&A, 381, L73

Kapahi V.K., Saikia D.J., 1982, JA&A, 3, 465

Kapahi V.K., Athreya R.M., van Breugel W., McCarthy P.J., Subrahmanya C.R., 1998a, ApJS, 118, 275

Kapahi V.K., Athreya R.M., Subrahmanya C.R., Baker J.C., Hunstead R.W., McCarthy P.J., van Breugel W., 1998b, ApJS, 118, 327

Karachentsev I.D., 1980, ApJS, 44, 137

Keel W.C., 1986, ApJ, 302, 296

Labiano A., O'Dea C.P., Gelderman R., et al., 2005, A&A, 436, 493

Large M.I., Mills B.Y., Little A.G., Crawford D.F., Sutton J.M., 1981, MNRAS, 194, 693

Leon S., Lim J., Combes F., Dinh-v-Trung, 2003, ASPC, 290, 525

Lim J., Leon S., Combes F., Dinh-V-Trung, 2000, ApJ, 545, 93L

Lister M.L., Kellermann K.I., Vermeulen R.C., Cohen M.H., Zensus J.A., Ros E., 2003, ApJ, 584, 135

Lüdke E., Garrington S.T., Spencer R.E., Akujor C.E., Muxlow T.W.B., Sanghera H.S., Fanti, C., 1998, MNRAS, 299, 467

McCarthy P.J., Kapahi V.K., van Breugel W., Persson S.E., Athreya R.M., Subrahmanya C.R., 1996, ApJS, 107, 19

Mirabel I.F., 1989, ApJ, 340, L13

Mirabel I.F., 1990, ApJ, 352, 37

Mirabel I.F., Sanders D.B., Kažes I., 1989, ApJ, 340, L9

Morganti R., Oosterloo T.A., et al., 2001, MNRAS, 323, 331

Morganti R., Oosterloo T.A., Tadhunter C.N., Vermeulen R., Pihlström Y.M., van Moorsel G., Wills K.A., 2004, A&A, 424, 119

Morganti R., Tadhunter C.N., Oosterloo T.A., 2005, *A&A*, 444, L9

Murphy D.W., Browne I.W.A., Perley R.A., 1993, *MNRAS*, 264, 298

Mutel R.L., Phillips R.B., Skuppin R., 1981, *AJ*, 86, 1600

Neff S.G., Roberts L., Hutchings J.B., 1995, *ApJS*, 99, 349

O'Dea C.P., 1998, *PASP*, 110, 493

Ojha R. et al., 2004, *AJ*, 127, 3609

Orr M.J.L., Browne I.W.A., 1982, *MNRAS*, 200, 1067

Owsianik I., Conway J.E., Polatidis A.G., 1998, *A&A*, 336, L37

Pearson T.J., Readhead A.C.S., 1988, *ApJ*, 328, 114

Peck A.B., Taylor G.B., 1998, *ApJ*, 502, 23

Peck A.B., Taylor G.B., Conway J.E., 1999, *ApJ*, 521, 103

Peck A.B., Taylor G.B., Fassnacht C.D., Readhead A.C.S., Vermeulen R.C., 2000, *ApJ*, 534, 104

Perlman E.S., Carilli C.L., Stocke J.T., Conway J., 1996, *AJ*, 111, 1839

Perlman E.S., Padovani P., Giommi P., Sambruna R., Jones L.R., Tzioumis A., Reynolds J., 1998, *AJ*, 115, 1253

Petrov L., Kovalev Y.Y., Fomalont E., Gordon D., 2005, *AJ*, 129, 1163

Phillips R.B., Mutel R.L., 1981, *ApJ*, 244, 19

Pihlström Y.M., 2001, PhD Thesis, Chalmers University of Technology

Pihlström Y.M., Conway J.E., Vermeulen R.C., 2003, *A&A*, 404, 871

Polatidis A.G., Wilkinson P.N., Xu W., Readhead A.C.S., Pearson T.J., Taylor G.B., Vermeulen R.C., 1995, *ApJS*, 98, 1

Rees M.J., 1984, *ARA&A*, 22, 471

Reid R.I., Kronberg P.P., Perley R.A., 1999, *ApJS*, 124, 285

Rines K., Geller M.J., Kurtz M.J., Diaferio A., 2003, *AJ*, 126, 2152

Röttgering H., Best P., Carilli C., Longair M., 1996, in Snellen I.A.G., Schilizzi R.T., Röttgering H.J.A., Bremer M.N., eds, The second workshop on gigahertz peaked spectrum and compact steep spectrum radio sources. Leiden Observatory, p. 48

Rupen M.P., 1997, in The nature of elliptical galaxies, eds M. Arnaboldi, G.S. Da Costa, P. Saha, *ASP Conf. Ser.*, 116, 322

Saikia D.J., Gupta N., 2003, *A&A*, 405, 499

Saikia D.J., Kulkarni A.R., 1998, *MNRAS*, 298, 45

Saikia D.J., Jeyakumar S., Wiita P.J., Sanghera H.S., Spencer R.E., 1995, *MNRAS*, 276, 1215

Saikia D.J., Jeyakumar S., Salter C.J., Thomasson P., Spencer R.E., Mantovani F., 2001, *MNRAS*, 321, 37

Saikia D.J., Thomasson P., Spencer R.E., Mantovani F., Salter C.J., Jeyakumar S., 2002, *A&A*, 391, 149

Sanders D.B., Soifer B.T., Elias J.H., Neugebauer G., Matthews K., 1988, *ApJ*, 328, 35

Sanghera H.S., Saikia D.J., Lüdke E., Spencer R.E., Foulsham P.A., Akujor C.E., Tzioumis A.K., 1995, *A&A*, 295, 629

Schilizzi R.T. et al., 2000, *AdSpR*, 26, 709

Scoville N.Z. et al., 2000, *AJ*, 119, 991

Snellen I.A.G., Lehnert M.D., Bremer M.N., Schilizzi R.T., 2002, *MNRAS*, 337, 981

Spencer R.E., McDowell J.C., Charlesworth M., Fanti C., 1989, *MNRAS*, 240, 657

Spencer R.E. et al., 1991, *MNRAS*, 250, 225

Spergel D.N., et al., 2003, *ApJS*, 148, 175

Spinrad H., Djorgovski S., Marr J., Aguilar L., 1985, *PASP*, 97, 932

Stanghellini C., Baum S.A., O'Dea C.P., Morris G.B., 1990, *A&A*, 233, 379

Stanghellini C., O'Dea C.P., Baum S.A., Laurikainen E., 1993, *ApJS*, 88, 1

Stanghellini C., O'Dea C.P., Murphy D.W., 1999, *A&AS*, 134, 309

Stanghellini C., Dallacasa D., O'Dea C.P., Baum S.A., Fanti R., Fanti C., 2001, *A&A*, 377, 377

Strom R.G., Riley J.M., Spinrad H., van Breugel W.J.M., Djorgovski S., Liebert J., McCarthy P.J., 1990, *A&A*, 227, 19

Taylor G.B., Vermeulen R.C., Pearson T.J., Readhead A.C.S., Henstock D.R., Browne I.W.A., Wilkinson P.N., 1994, *ApJS*, 95, 345

Taylor G.B., Vermeulen R.C., 1997, *ApJ*, 485, L9

Taylor G.B., Readhead A.C.S., Pearson T.J., 1996, *ApJ*, 463, 95

Taylor G.B., Wrobel J.M., Vermeulen R.C., 1998, *ApJ*, 498, 619

Taylor G.B., Marr J.M., Pearson T.J., Readhead A.C.S., 2000, *ApJ*, 541, 112

Thomasson P., Saikia D.J., Muxlow T.W.B., 2003, *MNRAS*, 341, 91

Tzioumis A. et al., 2002, *A&A*, 392, 841

Ulvestad J.S., Johnston K.J., Weiler K.W., 1983, *ApJ*, 266, 18

van Breugel W.J.M., Fanti C., Fanti R., Stanghellini C., Schilizzi R.T., Spencer R.E., 1992, *A&A*, 256, 56

van Gorkom J.H., Knapp G.R., Ekers, R.D., Ekers, D.D., Laing, R.A., Polk, K.S., 1989, *AJ*, 97, 708

van Ojik R., Röttgering H.J.A., Miley G.K., Hunstead R.W., 1997, *A&A*, 317, 358

Veilleux S., Sanders D.B., Kim D.C., 1997, *ApJ*, 484, 92

Venturi T., Morganti R., Tzioumis T., Reynolds J., 2000, *A&A*, 363, 84

Verdoes Kleijn G.A., Baum S.A., dw Zeew P.T., O'Dea C.P., 1999, *AJ*, 118, 2592

Vermeulen R.C. et al., 2003, *A&A*, 404, 861

Wall J.V., Peacock J.A., 1985, *MNRAS*, 216, 173

Walsh D.E.P., Knapp G.R., Wrobel J.M., Kim D.-W., 1989, *ApJ*, 337, 209

Wegner G., Haynes M.P., Giovanelli R., 1993, *AJ*, 105, 1251

Whyborn N.D., Browne I.W.A., Wilkinson P.N., Porcas R.W., Spinrad H., 1985, *MNRAS*, 214, 55

Wilkinson P.N., Tzioumis A.K., Benson J.M., Walker R.C., Simon R.S., Kahn F.D., 1991, *Nature*, 352, 313

Xiang L., Stanghellini C., Dallacasa D., Haiyan Z., 2002, *A&A*, 385, 768

Xu W., Readhead A.C.S., Pearson T.J., Polatidis A.G., Wilkinson P.N., 1995, *ApJS*, 99, 297

Zensus J.A., Ros E., Kellermann K.I., Cohen M.H., Vermeulen R.C., Kadler M., 2002, *AJ*, 124, 662